Microsecond photocapacitance transients observed using a charged microcantilever as a gated mechanical integrator
Short title: Microsecond photocapacitance transients

Ryan P. Dwyer,[1+] Sarah R. Nathan,[1+] John A. Marohn[1*]

[1]Department of Chemistry and Chemical Biology,
Cornell University, Ithaca, New York 14853-1301

[+]R.P.D. and S.R.N. contributed equally to this work.

[*]To whom correspondence should be addressed; E-mail: jam99@cornell.edu.

Summary sentence (125 characters max): A new way to measure the rate of light-induced charge generation in organic solar cell films with a nanometer-scale probe.

How light is converted to electricity in blends of organic donor and acceptor molecules is an unsettled question, in part because the spatial heterogeneity present in these blends makes them challenging to characterize. While scanned-probe measurements have provided crucially important microscopic insights into charge generation and transport in these blends, achieving the sub-nanosecond time resolution needed to directly observe the fate of photogenerated charges has proven difficult. Here we employ a charged microcantilever as a gated mechanical integrator to record photocapacitance indirectly by measuring the accumulated change in cantilever phase as a function of the time delay between precisely synchronized voltage and light pulses. In contrast with prior time-resolved scanned-probe photocapacitance measurements, the

time resolution of this method is set by the rise and fall time of the voltage and light pulses and not by the inverse detection bandwidth. We demonstrate in an organic donor-acceptor blend the ability of this indirect, "phase kick" technique to record multi-exponential photocapacitance transients on timescales ranging from 40 microseconds to 10 milliseconds. The technique's ability to measure subcycle, nanosecond charge dynamics is demonstrated by measuring the 10s of nanosecond sample electrical charging time.

Introduction

We introduce a method that significantly improves the time resolution of electric force microscopy, enabling the rapid acquisition of photocapacitance transients in solar-cell films. A light pulse generates free carriers in the sample while a nearby charged microcantilever is used as a voltage-gated mechanical integrator to encode the time evolution of the subsequent carrier recombination as a change in the cantilever's phase of oscillation. We illustrate the method by using it to reveal a biexponential photocapacitance buildup in a polymer-blend solar-cell film, with the fast component having a risetime of $40\,\mu\mathrm{s}$ at high light intensity. We demonstrate the method's time resolution in a control experiment in which we measure a tip-charging time of $35\,\mathrm{ns}$.

Scanned probe microscopy has allowed researchers to explore spatial variations in charge generation and transport in solar-cell films prepared on a conductive substrate (*1–4*) with a best-case resolution of $2\,\mathrm{nm}$ (*5*). Ginger and coworkers introduced time-resolved electric force microscopy (tr-EFM) which enabled the study of photocapacitance transients on the microsecond timescale in bulk heterojunction organic blends (*6–9*). These studies revealed that photocapacitance charging rates were proportional to external quantum efficiency in prototypical organic bulk heterojunction blends, raising the exciting possibility of using scanned-probe mi-

croscope measurements to help rationally optimize the processing of organic semiconductor donor-acceptor blends.

We seek to extend the time resolution of electric force microscopy (EFM) in order to study fundamental processes like photoinduced electron transfer, charge recombination, charge trapping, photocatalysis, and ferroelectric switching, at the single-molecule or single-domain level. Such studies would help us understand the mechanism of charge generation (*10–21*) and recombination (*12, 18, 22, 23*) in organic donor-acceptor blends, for example — a topic of intense debate. Nanosecond-resolution microwave conductivity measurements of charge generation have recently revealed tantalizing evidence that Marcus theory can be applied to understand charge generation in an organic donor-acceptor photovoltaic film (*12, 24*). The ability to perform analogous EFM measurements at high spatial resolution on conductive substrates is therefore an extremely exciting possibility. Frustratingly, the tr-EFM experiment's time resolution is set by the detector and demodulation bandwidth; achieving nanosecond time resolution would seem to require using radiofrequency oscillators digitized at GHz sampling rates, which is impractical.

To impart EFM with nanosecond resolution we must rethink the experiment from first principles. Ultrafast indirect scanning tunneling microscopy (STM) measurements have demonstrated ns to ps time resolution on gallium arsenide, but these measurements lack the clear connection to organic solar cell performance demonstrated by Ginger *et al.* with tr-EFM (*25–32*). Indirect Kelvin probe force microscopy (KPFM) methods can measure surface potential changes with picosecond time resolution (*33–37*), but these measurements exploit the nonlinear dependence of photovoltage on light intensity and/or the nonlinear dependence of the cantilever frequency f_c on photovoltage or assume the tip voltage passively observes sample properties. Unfortunately, because photocapacitance generally depends linearly on light intensity, produces a linear change in f_c, and depends *strongly* on tip voltage, the ultrafast methods of Refs. 33–37 are not applicable to the donor-acceptor blends studied here.

In this work, we demonstrate a new method to measure the photocapacitance charging rate — "phase-kick" electric force microscopy (pk-EFM). The pk-EFM measurement is sensitive to the same underlying photocapacitance dynamics as Ginger's tr-EFM measurement. Our measurement employs an indirect, non-linear detection protocol that enables the reconstruction of the full photocapacitance transient while sidestepping detector-noise and demodulator-bandwidth limitations to the achievable time resolution.

Photocapacitance measurements. We bring a conductive cantilever near an organic donor-acceptor semiconductor film (PFB:F8BT, see Fig. 1A). A voltage pulse is applied to the cantilever while a carefully timed light pulse is applied to the sample.

Due to electrostatic interactions with the sample, the cantilever's resonance frequency is shifted by

$$\delta f(t) = -\frac{f_0}{4k_0} C''_{\mathrm{t}}(t, h\nu)\big(V_{\mathrm{t}} - \Phi(t, h\nu)\big)^2, \tag{1}$$

where f_0 and k_0 are the cantilever resonance frequency and spring constant, respectively; V_{t} is the tip voltage; Φ is the sample's surface potential; and C''_{t} is the second derivative of the tip-sample capacitance with respect to the vertical direction. We write $C''_{\mathrm{t}}(t, h\nu)$ and $\Phi(t, h\nu)$ to indicate that these quantities depend on time and light through the sample's photocapacitance and photopotential, respectively. The change in the curvature of the δf *vs.* V_{t} parabola apparent in Fig. 1B indicates that, in the PFB:F8BT sample, light primarily affects C'' and not Φ.

To measure the time evolution of the sample's photocapacitance in Fig. 1, the tip voltage was fixed at $V_{\mathrm{t}} = 10\,\mathrm{V}$ and the cantilever frequency shift was recorded following the application of a light pulse. The large tip-sample voltage $V_{\mathrm{ts}} - \Phi$ makes the measurement relatively insensitive to light-induced changes in Φ. In the representative data of Fig. 1C, the photocapacitance charging time is $\tau \sim 5\,\mathrm{ms}$. In Fig. 1D we show that photoinduced changes in C''_{t} persist for many seconds, making it difficult or impossible to collect reproducible data and implement signal

averaging. As previously observed by Coffey and Ginger (*6, 38*), we found that C_{t}'' could be induced to recover quickly by returning the tip voltage to zero, which sweeps out charge accumulated below the tip (Supplementary text 1, Fig. S1).

Experimental protocol. Figure 2 shows our new, indirect photocapacitance measurement. We oscillate the cantilever at its resonance frequency using a commercial phase-locked loop controller (Fig. 2A). Since the cantilever resonance peak in vacuum is narrow ($\Delta f_{\mathrm{FWHM}} = 2.5\,\mathrm{Hz}$), we turn off the cantilever drive at $t = -10\,\mathrm{ms}$ so that analysis of the photocapacitance transients is not complicated by phase-locked-loop phase errors (Fig. 2B). We apply precisely timed voltage steps and light pulses using a commercial pulse and delay generator. To begin the experiment, we step the tip-sample voltage from $V_{\mathrm{t}} = \Phi$ to $V_{\mathrm{t}} = \Phi + 10\,\mathrm{V}$ (Fig. 2C). Over the next $50\,\mathrm{ms}$, tip-sample charge equilibrates as additional electrons flow to the sample surface. The additional electrons increase the magnitude of the cantilever frequency shift from approximately $\delta f(-50\,\mathrm{ms}) = -133\,\mathrm{Hz}$ to $\delta f(0) = -150\,\mathrm{Hz}$ (Fig. 2D).

At $t = 0$, we apply a light pulse synchronized to the cantilever oscillation (Fig. 2D). The light pulse initiates charge generation, which causes a change in the capacitance derivative C_{t}'' (Fig. 2E). This change induces a small shift in the cantilever's frequency of oscillation (Fig. 2F). The frequency shift concomitantly advances the cantilever's *phase* of oscillation. At a time $t = t_{\mathrm{p}}$, we arrest the photo-induced advance of the cantilever phase by abruptly stepping the tip voltage back to zero (Fig. 2C):

$$V_{\mathrm{t}}(t) = \begin{cases} V & \text{for } \; t < t_{\mathrm{p}} \\ 0 & \text{for } \; t \geq t_{\mathrm{p}}. \end{cases} \tag{2}$$

In these experiments, we end the light pulse and the voltage step simultaneously to limit the sample's exposure to high light intensities (Fig. 2G). This synchronization is not critical for the measurement, however. No matter when the light pulse ends, $\delta f \approx 0$ after the voltage turns off because $V_{\mathrm{t}} \approx \Phi$. After the voltage turns off, we wait a delay time t_{d} before restoring the

phase-locked loop drive. We wait at least $5\,\mathrm{ms}$ so that the data used to determine the cantilever phase at the end of the light pulse is not complicated by phase-locked-loop phase errors ($t_\mathrm{d} = 5$ to $15\,\mathrm{ms}$).

Figure 2H through 2M shows how the we calculate the phase shift $\Delta\phi = \phi(t_\mathrm{p}) - \phi(0)$. We measure cantilever displacement using a fiber interferometer, digitally sample the displacement at $1\,\mathrm{MHz}$, and save the full transient for later analysis. We first process the cantilever displacement data using a software lock-in amplifier and determine the cantilever frequency before the beginning of the pulse and after the end of the pulse using $3.4\,\mathrm{ms}$ and $6\,\mathrm{ms}$ of data, respectively (the highlighted region of Fig. 2F; see supplementary text 2 to 4). We use these frequencies to construct a second software lock-in amplifier with a variable reference frequency set to match the cantilever frequency before and after the pulse. From the in-phase and out-of-phase channels of the lock-in amplifier, we determine the cantilever amplitude, frequency, and phase. Setting the lock-in amplifier to match the cantilever's expected frequency before and after the light pulse isolates the effect of the photo-induced change in capacitance (compare Fig. 2F and K).

The net phase shift $\Delta\phi$ is the time integral of the light-induced change in the cantilever frequency (Fig. 2K, shaded region). The frequency shift, and hence the phase shift, depends on the product of the sample's capacitance and the square of the tip voltage (Eq. 1). By pulsing the tip voltage we turn the cantilever into a *gated mechanical integrator* of the photocapacitance transient. We step the time t_p, repeat the experiment, and plot the net cantilever phase shift $\Delta\phi$ versus t_p (Fig. 2M). The measured phase shift is proportional to the integrated photocapacitance transient,

$$\Delta\phi = \int_0^{t_\mathrm{p}} \delta f(t)\,dt = -\frac{f_0}{4k_0} V^2 \int_0^{t_\mathrm{p}} C''_\mathrm{t}(t, h\nu)\,dt \tag{3}$$

We fit the measured $\Delta\phi$ *versus* t_p curve to learn about the sample's transient photocapacitance.

In Fig. 3 we present an alternative view of the pk-EFM experiment. At the top of the fig-

ure we plot *versus* time the sinusoidal cantilever-displacement oscillation and, for comparison, a square-wave reference oscillation. With the light off, the cantilever and reference oscillator evolve in sync. Turning on the light causes the cantilever to begin oscillating at a lower frequency (Fig. 3, top middle) such that, by the time the illumination is halted, the cantilever's phase of oscillation has shifted relative to that of the reference oscillator (Fig. 3, top right). At the bottom of Fig. 3 we show the evolution of the cantilever and reference oscillator as viewed in phase space and at the outputs of a lock-in detector. At long times (Fig. 3, lower right), the observed phase difference is blurred by phase noise in the cantilever oscillation, but the average phase difference is still retained.

pk-EFM Theory

To demonstrate that our new technique is sensitive to subcycle, nanosecond dynamics, we model the cantilever as a harmonic oscillator with position x, momentum p, mass m, and spring constant k_0,

$$\dot{x} = p/m \tag{4}$$

$$\dot{p} = -(k_0 + \delta k(t))\, x + F(t) \tag{5}$$

with,

$$F(t) = \frac{1}{2} C_{\mathrm{t}}'(t) V_{\mathrm{t}}(t)^2 \tag{6}$$

$$\delta k(t) = \frac{1}{2} C_{\mathrm{t}}''(t) V_{\mathrm{t}}(t)^2, \tag{7}$$

a time-dependent force and spring-constant shift, respectively, caused by the capacitive tip-sample interaction. In Eq. 7, C_{t}' and C_{t}'' are the first and second derivatives of the tip-sample capacitance with respect to height and V_{t} is the tip voltage. We neglect dissipation because

the experiments described here occur on a timescale much shorter than the cantilever ringdown time. Equations 4 and 5 are two coupled linear equations with time-dependent coefficients.

Magnus expansion. While there is no general analytic solution to Eqs. 4 and 5, we can use the Magnus expansion to obtain a highly accurate approximate solution (*39, 40*). The cantilever's evolution can be written in terms of the state vector $\boldsymbol{x} = (x\ p)^T$,

$$\dot{\boldsymbol{x}} = \boldsymbol{A}(t)\boldsymbol{x} + \boldsymbol{b}(t), \tag{8}$$

with a state matrix

$$\boldsymbol{A}(t) = \begin{pmatrix} 0 & 1/m \\ -m\omega_0^2\,(1+\kappa(t)) & 0 \end{pmatrix} \tag{9}$$

and generalized force

$$\boldsymbol{b}(t) = \begin{pmatrix} 0 \\ F(t) \end{pmatrix}. \tag{10}$$

We write $\boldsymbol{A}$ using the cantilever resonance frequency $\omega_0 = \sqrt{k_0/m}$ and the normalized spring-constant shift

$$\kappa(t) \equiv \delta k(t)/k_0. \tag{11}$$

The exact solution for the time evolution of the state vector in Eq. 8 can be written in terms of the system's propagator $\boldsymbol{U}$,

$$\boldsymbol{x}(t) = \boldsymbol{U}(t,t_0)\,\boldsymbol{x}(t_0) + \int_{t_0}^{t} \boldsymbol{U}(t,t')\,\boldsymbol{b}(t')\,dt'. \tag{12}$$

The Magnus expansion writes the propagator as the exponential of a certain matrix $\boldsymbol{\Omega}$, $\boldsymbol{U}(t,t_0) \equiv \exp \boldsymbol{\Omega}(t,t_0)$. The first-order Magnus approximation for $\boldsymbol{\Omega}$ is

$$\boldsymbol{\Omega}(t,t_0) \approx \int_{t_0}^{t} \boldsymbol{A}(t')dt'. \tag{13}$$

This gives the approximate propagator

$$\boldsymbol{U}(t,t_0) \approx \begin{pmatrix} \cos\left(\bar{\omega}\,(t-t_0)\right) & (m\,\bar{\omega})^{-1}\sin\left(\bar{\omega}\,(t-t_0)\right) \\ -m\,\bar{\omega}\sin\left(\bar{\omega}\,(t-t_0)\right) & \cos\left(\bar{\omega}\,(t-t_0)\right) \end{pmatrix}, \tag{14}$$

where $\bar{\omega}(t,t_0)$ is a *time-dependent frequency* representing the average cantilever frequency between the time t_0 and t,

$$\bar{\omega}(t,t_0) = \omega_0\left(1+\frac{1}{t-t_0}\int_{t_0}^{t}\kappa(t')\,dt'\right)^{1/2}. \tag{15}$$

Likewise, $\theta(t,t_0) = \bar{\omega}\,(t-t_0)$ is the cantilever phase accumulated between t_0 and t. Typically $\kappa \ll 1$ so the phase is well-approximated by

$$\theta(t,t_0) \approx \omega_0\,(t-t_0) + \frac{\omega_0}{2}\int_{t_0}^{t}\kappa(t')\,dt'. \tag{16}$$

Equation 1, the usual KPFM expression for the cantilever's frequency, is recovered by defining an instantaneous frequency $2\pi f(t) = d\theta/dt$.

Experimental protocol. Consider the experiment of Fig. 2. We abruptly initiate sample illumination at time $t = 0$, and the sample's capacitance begins evolving to a new steady-state value. Simultaneously, both C_{t}' and C_{t}'' will likewise evolve to new values, following the same dynamics. The key to extracting the photocapacitance transient is that we can independently control the tip voltage $V_{\mathrm{t}}(t)$. At a subsequent time $t = t_{\mathrm{p}}$, we abruptly turn the tip voltage to zero as in Eq. 2. Inserting Eqs. 2 and 7 into Eq. 11 and inserting the result into Eq. 16 with $t_0 = 0$, we obtain

$$\theta \approx \omega_0\,t - \frac{\omega_0 V^2}{4k_0}\int_0^{t_{\mathrm{p}}} C_{\mathrm{t}}''(t')\,dt', \tag{17}$$

which agrees with the phase shift given in Eq. 3.

Long time response. For simplicity let us model the photocapacitance dynamics as single-exponential with a risetime of τ. In this approximation $C_{\mathrm{t}}''(t) = C_{\mathrm{t}}''(0) + \Delta C_{h\nu}''(1-e^{-t/\tau})$ for

$t > 0$. Inserting this $C_{\rm t}''(t)$ into Eq. 17, we obtain the cantilever phase measured at $t \geq t_{\rm p}$,

$$\theta(t) \approx \omega_0\, t - \frac{\omega_0 V^2}{4k_0} \Delta C_{\rm t}''(0)\, t_{\rm p} + \Delta\phi \tag{18}$$

$$\Delta\phi = -\frac{\omega_0 V^2}{4k_0} \Delta C_{h\nu}'' \left\{ t_{\rm p} - \tau + \tau\, e^{-t_{\rm p}/\tau} \right\}. \tag{19}$$

The first term in this equation, $\omega_0\, t$, is the expected time-dependent phase arising from free evolution of the cantilever. The second term is a pulse-time-dependent phase shift arising from the voltage-dependent force gradient. Since both ω_0 and $\Delta C_{\rm t}''(0)$ are easily measured, it is straightforward to extract from θ the additional phase shift $\Delta\phi$ arising from the transient photocapacitance. The slope of the $\Delta\phi$ *versus* $t_{\rm p}$ line is $-\omega_0 V^2 \Delta C_{h\nu}''/(4k_0)$ and the intercept is τ, the sample's sought-after photocapacitance risetime.

Short time response. At short times, the forcing term $\boldsymbol{b}(t)$ in Eq. 8 also contributes significantly to the cantilever's subsequent motion. We model the $C_{\rm t}'$ photocapacitance dynamics with the same single-exponential risetime τ: $C_{\rm t}'(t) = C_{\rm t}'(0) + \Delta C_{h\nu}'(1 - e^{-t/\tau})$. For reference, consider the effect of this force in the absence of photocapacitance ($\Delta C_{h\nu}' = 0$). The electrostatic force vanishes abruptly at time $t = t_{\rm p}$, so that the cantilever's position and momentum evolve according to the equations

$$\begin{pmatrix} x(t \geq t_{\rm p}) \\ p(t \geq t_{\rm p}) \end{pmatrix} = \begin{pmatrix} A_0 \cos\left(\omega_0(t - t_{\rm p}) + \phi_{\rm p}\right) + \delta x_0 \cos\left(\omega_0(t - t_{\rm p})\right) \\ -m\omega_0 A_0 \sin\left(\omega_0(t - t_{\rm p}) + \phi_{\rm p}\right) \end{pmatrix} = \boldsymbol{U}(t, t_{\rm p}) \begin{pmatrix} A_0 \cos\phi_{\rm p} + \delta x_0 \\ -m\omega_0 A_0 \sin\phi_{\rm p} \end{pmatrix} \tag{20}$$

with $\delta x_0 = V^2 C_{\rm t}'(0)/(2k_0)$ the DC deflection of the cantilever due to the electrostatic force on the tip and $\phi_{\rm p} = \theta(t_{\rm p})$ the cantilever's phase at $t_{\rm p}$, given by Eq. 18. For $\delta x_0 \ll A_0$, the effect of δx_0 on x in a voltage-only reference experiment can be written in terms of an equivalent shift in amplitude and phase given by, respectively,

$$\Delta A_{\rm ref} = \quad \delta x_0 \cos\phi_{\rm p} \tag{21}$$

$$\Delta\phi_{\rm ref} = -\frac{\delta x_0}{A_0} \sin\phi_{\rm p}. \tag{22}$$

In words, the $V_{\rm t} \rightarrow 0$ step leads to either an amplitude or phase shift depending on the cantilever's absolute phase of oscillation at the moment when the voltage is returned to zero.

The photocapacitance term $\Delta C'_{h\nu}$ adds an additional shift to the cantilever position and momentum

$$\begin{pmatrix} \Delta x_{h\nu}(t \geq t_{\rm p}) \\ \Delta p_{h\nu}(t \geq t_{\rm p}) \end{pmatrix} \simeq \delta x_{h\nu} \frac{\omega_0}{1+\tau^2\omega_0^2} \left\{ t_{\rm p} - \tau + \tau e^{-t_{\rm p}/\tau} \right\} \boldsymbol{U}(t, t_{\rm p}) \begin{pmatrix} \tau\omega_0 \\ -m\omega_0 \end{pmatrix}. \tag{23}$$

with $\delta x_{h\nu} = V^2 \, \Delta C'_{h\nu}/(2k_0)$ the DC deflection arising from the photocapacitance-related force. In writing Eq. 23, we have used the approximation that we are working in a short-time limit where $t_{\rm p} \ll 1/\omega_0$ and $\tau \ll 1/\omega_0$. The shifts in position and momentum in Eq. 23 should be added to Eq. 20. The resulting change in cantilever position can be written in terms of an additional amplitude and phase shift. For $\tau\omega_0 \ll 1$, the effect of $\Delta x_{h\nu}$ on the amplitude and phase is small compared to the effect of $\Delta p_{h\nu}$. In this limit,

$$\Delta A \simeq -\frac{\Delta p_{h\nu}}{m\omega_0} \sin\phi_{\rm p} \tag{24}$$

$$\Delta\phi \simeq -\frac{\Delta p_{h\nu}}{A_0 m\omega_0} \cos\phi_{\rm p}. \tag{25}$$

Writing the amplitude and phase shifts out, we have

$$\Delta A \simeq \delta x_{h\nu} \frac{\omega_0}{1+\tau^2\omega_0^2} \left\{ t_{\rm p} - \tau + \tau e^{-t_{\rm p}/\tau} \right\} \sin\phi_{\rm p} \tag{26}$$

$$\Delta\phi \simeq \frac{\delta x_{h\nu}}{A_0} \frac{\omega_0}{1+\tau^2\omega_0^2} \left\{ t_{\rm p} - \tau + \tau e^{-t_{\rm p}/\tau} \right\} \cos\phi_{\rm p}. \tag{27}$$

Remarkably, the braced terms in Eqs. 23, 26 and 27 show the same characteristic dependence on τ seen in the long-time phase-shift experiment, Eq. 19. By controlling the timing of the voltage pulse we can arrange for $\phi_{\rm p}$ to be $\pi/2$; in this case the short-time photocapacitance leads to a phase shift. We can instead encode the short-time photocapacitance as an amplitude shift by adjusting the pulse time so $\phi_{\rm p} = 0$ or π. Below we demonstrate the use of an amplitude shift to verify the effect of short ($< 1\,\mu$s) duration voltage pulses on the cantilever. The slope

of the $\Delta\phi$ *versus* t_p line is $\omega_0 V^2 \Delta C'_{h\nu}/(2A_0 k_0)$. We observe that $\Delta C'_{h\nu}/A_0 \gg \Delta C''_{h\nu}$, making the accumulated phase per unit time in the short-time experiment an order of magnitude larger than one would expect from extrapolating Eq. 18. This fortuitous finding partially mitigates the challenge of observing the small total phase shift accumulated in a sample with submicrosecond photocapacitance dynamics.

Results

See the Materials and Methods section for a description of sample-fabrication, measurement, and data-analysis protocols.

We directly compared the new phase-kick technique outlined in Figure 2 to tr-EFM by performing both experiments consecutively, under identical illumination and sample conditions ($I_{h\nu} = 100\,\mathrm{kW\,m^{-2}}$, PFB:F8BT on ITO). For the pk-EFM experiment, we measured phase shift $\Delta\phi$ *vs.* pulse time t_p for $N = 768$ data points with the pulse time varied from 0 to $1.4\,\mathrm{ms}$. For each pulse time, we also collected a control data point with the light off. For the tr-EFM experiment, we calculated the mean and standard error of the frequency shift δf *vs.* time t from $N = 384$ repetitions. For both experiments, an $87\,\mathrm{ms}$ delay (with $V_\mathrm{t} = 0\,\mathrm{V}$) was included between repetitions to ensure the sample's photocapacitance was fully recovered. We operate at a tip-sample separation of $h = 250\,\mathrm{nm}$ to limit the effects of tip-sample drift over the course of the 20 minute measurement. To compare the two experiments, we modeled the cantilever's frequency shift under illumination as the sum of two exponentials,

$$\delta f(t) = \Delta f_1(1 - e^{-t/\tau_1}) + \Delta f_2(1 - e^{-t/\tau_2}). \tag{28}$$

The tr-EFM mean frequency shift data was fit directly to Equation 28. Since the phase shift during the pulse is the integral of the frequency shift (Eq. 3), we fit the phase to the integral of Equation 28.

We fit to a biexponential model because the data fits a single exponential model poorly (supplementary text 5, figure S5). A biexponential model offers enough degrees of freedom to adequately fit our data. Since we do not yet have a microscopic model for photocapacitance, as explained in the Discussion section, we will not speculate on the physical origin of the two components. We conclude only that the measured frequency shift has both a fast and slow component. A successful microscopic model would explain our observation of a fast initial change in capacitance and continued slow changes in capacitance that extend for much longer than a single exponential model would predict.

We can nevertheless rule out several possibilities for the observed biexponential frequency and phase transients. At the highest light intensities, the changes in photocapacitance are fast enough to potentially involve our short time response theory (Eqs. 20–27). We do see evidence that light-induced changes in the tip-sample force $F \propto C_{\mathrm{t}}'$ affect the cantilever phase, but the size of the neglected phase shift is only $\sim 0.2\,\mathrm{mcyc}$, small compared to the total measured phase shift (supplementary texts 6 and 7, figure S6). The measured power spectral density of the cantilever displacement signal shows no evidence that multi-modal excitation occurs during our experiments (supplementary text 8 and Figs. S7 and S8). The cantilever's surface potential Φ shifted by $+160$ to $+440\,\mathrm{mV}$ under illumination (from $0.1\,\mathrm{kW\,m^{-2}}$ to $100\,\mathrm{kW\,m^{-2}}$ intensity). Since we operated at a positive tip voltage, this light-induced surface potential shift would, in isolation, produce a *positive* cantilever frequency or phase shift. This positive shift is inconsistent with the negative frequency shift of the fast component. It is unlikely, therefore, that the fast component arises from a photovoltage transient.

In Fig. 4A, we compare the datasets by plotting the pk-EFM phase shift experimental and control data along with the integrated biexponential best fit calculated from both the pk-EFM and tr-EFM experiments. The gray points show the control data before correcting for the phase shift caused by the abrupt change in tip-sample voltage at the end of the pulse (Eq. 22, see

supplementary text 4). In Fig. 4B, the raw tr-EFM data is compared to the biexponential best fit calculated from both the phasekick and tr-EFM experiments. Even though the two fits come from different datasets, they are quite consistent. The agreement between the plots in Fig. 4A and B establishes that both techniques measure the same photocapacitance information.

To further demonstrate the equivalent information obtained with the two techniques, we repeated this direct comparison at light intensities ranging from 0.1 to $100\,\mathrm{kW\,m^{-2}}$. The pk-EFM results are shown in Fig. 4C. The time constant is different at each light intensity. The best-fit time constants τ_1, τ_2 are found to be comparable for the two methods across the full range of intensities (Fig. 4D, Fig. S5). For the fast τ_1 time constants measured at $20\,\mathrm{kW\,m^{-2}}$ and $100\,\mathrm{kW\,m^{-2}}$, the time constants and error bars are less directly comparable. The tr-EFM model does not account for the fact that the measured $\Delta f(t)$ is a convolution of the cantilever's actual frequency shift with the lock-in amplifier filter (see Fig. 7A), which explains why it measures longer time constants. The pk-EFM error bars are moreover highly dependent on the pulse times used; to better measure the very fast component of the $20\,\mathrm{kW\,m^{-2}}$ data set, for example, more data points could be taken for pulse times from 0 to $100\,\mu\mathrm{s}$. Consistent with Coffey *et al.*, the time constants decrease with increasing intensity (*6*).

Coffey *et al.* only employed light intensities up to $2.5\,\mathrm{kW\,m^{-2}}$. In agreement with Coffey *et al.*, we see very little dependence of Δf_∞ on intensity at low intensities ($< 2.5\,\mathrm{kW\,m^{-2}}$). At higher intensities, we find that Δf_∞ increases with increasing intensity (Fig. S12). The light-induced surface potential change ($\Delta\Phi_{h\nu}$ increasing from $+160$ at $0.1\,\mathrm{kW\,m^{-2}}$ to $+440\,\mathrm{mV}$ at $100\,\mathrm{kW\,m^{-2}}$) would, on its own, lead to a decrease in Δf_∞ with increasing light intensity. The change in Δf_∞ is also unlikely to be due to photothermal effects; we estimate that sample heating caused by the laser at $I_{h\nu} = 100\,\mathrm{kW\,m^{-2}}$ is $2\,\mathrm{K}$ during the $1.5\,\mathrm{ms}$ pulse time (supplementary text 9).

Figure 4 shows that we can measure sample dynamics down to the very edge of the long-

time response limit with pk-EFM. In the long-time response limit, the difference between pk-EFM and tr-EFM is not dramatic. Before proceeding to the short-time response limit, it is helpful to write a simple model of the measurement. When we turn on the light, the cantilever's *actual* frequency δf_{cant} changes as a function of time. The changes in the cantilever's actual frequency are related to the sample's response function G_{samp}. We write the *actual* cantilever frequency shift δf_{cant} as a convolution (denoted by $*$) of the sample response function G_{samp} and a dummy variable u representing the light intensity:

$$\delta f_{\mathrm{cant}}(t) \propto (u * G_{\mathrm{samp}})(t). \tag{29}$$

In tr-EFM or pk-EFM, we attempt to infer information about sample properties (G_{samp}) from the cantilever's *measured* frequency (or phase) shift δf_{meas}. The measured frequency shift δf_{meas} or phase shift $\delta\phi_{\mathrm{meas}}$ is the convolution of the lock-in amplifier response function H_{L} and the cantilever's actual frequency shift:

$$\delta f_{\mathrm{meas}}(t) = (H_{\mathrm{L}} * \delta f_{\mathrm{cant}})(t). \tag{30}$$

In a typical direct measurement, it is assumed that sample dynamics are significantly slower than the time scale of the lock-in amplifier response, so that $\delta f_{\mathrm{meas}}(t) \approx \delta f_{\mathrm{cant}}(t)$.

In Figure 5, we attempt to use tr-EFM to measure the sample's fast charging time τ_{c}. We step the cantilever tip voltage from $V_{\mathrm{t}} = \Phi$ to $V_{\mathrm{t}} = \Phi + 10\,\mathrm{V}$ (A). The sought-after charging time τ_{c} is a property of the sample response function G_{samp} (B). We signal-average $N = 784$ steps, all precisely synchronized to the cantilever oscillation cycle. We demodulate the signal-averaged data with a wide bandwidth lock-in amplifier filter H_{L} (C, $\omega_{\mathrm{L}}^{-1} = 20\,\mu\mathrm{s}$). We expect that the cantilever's actual frequency δf_{cant} quickly changes as the sample charges on the microsecond or faster timescale. However, the measured frequency shift δf_{meas} and phase evolve over a timescale of 10s of microseconds, reflecting the time scale of the lock-in amplifier filter H_{L}. We also observe a significant change in cantilever amplitude, Fig. 5D, which only occurs when

the charging time occurs on a timescale similar to or faster than the inverse cantilever frequency: $\tau_c \leq \omega_c^{-1} = 2.6\,\mu s$ (Equation S13). However, the timescale of the change in the cantilever's measured amplitude is dominated by the response of the lock-in amplifier filter. To demonstrate the difficulty of inferring information about sample properties from the measured amplitude and frequency, we model the expected cantilever amplitude for sample charging time constants of $\tau_c = 0.1\,\mathrm{ns}$ (orange) and $\tau_c = 1000\,\mathrm{ns}$ (purple). The residuals for the two models are shown in Figure 5E. Since $\tau_c \ll \tau_L$, there is essentially no difference in the cantilever's measured amplitude *versus* time even over this 4 order of magnitude range of sample charging times. Using the demodulated phase $\delta\phi_{meas}$ offers no improvement; the phase *versus* time transient exhibits the same characteristic broadening due to the convolution of the actual phase $\delta\phi_{cant}$ with the lock-in amplifier filter.

The bandwidth of the lock-in amplifier measurement $b_L = 8\,\mathrm{kHz}$ is much lower than the bandwidth of our detector $b_{det} = 200\,\mathrm{kHz}$. With the results of our short time response theory available (Eqs. 20–27), it is natural to consider measuring the light-induced shifts in cantilever position directly in the time domain. We fit the same signal-averaged displacement *versus* time data for $t < 0$ (J, blue curve). In Figure 5K, we plot the difference between the measured displacement data and the blue curve fit. This difference corresponds to the additional cantilever displacement caused by the fast change in tip-sample force F (Equations 12 and S13). We model the charging-induced oscillation and plot the fits and residuals (L) for $\tau_c = 10\,\mathrm{ns}$ (orange, circles) and $\tau_c = 350\,\mathrm{ns}$ (purple, squares). There is effectively no difference in the cantilever's displacement for $\tau_c = 350\,\mathrm{ns}$ (2 percent of the cantilever period) or faster. This result puts a hard limit on the time resolution of tr-EFM or FF-trEFM; if two different sample time constants produce identical cantilever position *versus* time data, no amount of post-processing can distinguish between them.

Figure 6 shows a pk-EFM measurement of a submicrosecond charging time constant. We

applied ($< 1\,\mu s$) voltage pulses to the cantilever tip on $N = 100$ consecutive cantilever oscillation cycles (A). The demodulated cantilever amplitude, frequency and phase are plotted in Figure 6B–D. Figure 6E shows that the pulses shift the cantilever amplitude or phase, depending on the phase of the cantilever at the time of the voltage pulse. The magnitude of the amplitude or phase shift is related to the pulse time t_p. For instantaneous sample charging, we would expect $\Delta A_{max} \propto t_p$. Figure 6F shows that the magnitude of $\Delta A_{max}/t_p$ diminishes for short pulse times, consistent with charge being unable to get in and out of the sample on the timescale of the fastest pulses. From $t_p = 50\,ns$ to $t_p = 800\,ns$, the magnitude of the sample's response changes by a factor of 2. The two points on the left of Figure 6F show the measured amplitude response leveling off for t_p between 400 and $800\,ns$. For tr-EFM, however, the measured amplitude change only levels off on the timescale of the lock-in amplifier filter, $10s$ of μs (Figure 5D). Even measured directly in the time-domain, the cantilever takes an order of magnitude longer ($\sim 5\,\mu s$) to fully reflect the effect of the voltage pulse. The key difference is that in pk-EFM, a tip voltage pulse of length t_p effectively probes the average value of the sample response G_{samp} over the interval $t = 0$ to t_p. This is dramatically different from the tr-EFM measurement of Figure 5D–F, where the measured amplitude, frequency, or phase at a given point in time is always averaged over the width of the lock-in amplifier filter. Crucially, in pk-EFM the measured phase or amplitude shift is *independent* of the lock-in amplifier or detector. This can be seen clearly in the data of Figure 6C, where the same data is demodulated with two different bandwidths. While the shape and smoothness of the traces in Figure 6C is different, the integrated frequency shift or phase shift shown in Figure 6D is the same. The only caveat is that the limits of the integral must be extended appropriately to account for the rise and fall time of the lock-in amplifier filter.

To quantitatively describe the experiment of Figure 6A–F, we account for the finite charging and discharging time of the sample in response to a square pulse by writing $V_t(t) = V(1 -$

e^{-t/τ_c}) for $t \in (0, t_p)$ and $V_t(t) = V(1 - e^{-t_p/\tau_c})e^{-(t-t_p)/\tau_c}$ subsequently, where V is the amplitude of the square pulse, τ_c the effective sample charging time and t_p the duration of the square pulse. Reworking the derivation of the amplitude jump from this starting point gives $\Delta A/t_p = \delta x_c \sin\phi_p \left(1 - \tau_c t_p^{-1} - \tau_c t_p^{-1} e^{-t_p/\tau_c}\right)$ with the phase shift $\phi_p = 2\pi f_0 t_d$ controlled by the pulse time delay t_d and $\delta x_c = V^2 C_t'/(2k_0)$ a DC deflection due to electrostatic forces. The measured cantilever amplitude change in Fig. 6E shows the expected sinusoidal dependence on delay time. Figure 6F shows that the $\Delta A/t_p$ *vs.* t_p data is well described by the above equation with $\tau_c = 34 \pm 5\,\mathrm{ns}$.

To provide evidence that pk-EFM can likewise measure nanosecond photocapacitance dynamics, we simulated cantilever dynamics using a model similar to Equations 4–7. The simulations included independently measured effects from (a) near-surface cantilever frequency fluctuations (*41–43*), (b) thermal fluctuations in cantilever position (*44*), (c) detector noise (*42*), and (d) transient force and force gradients arising from the gated photocapacitance signal. Representative numerical simulations assuming 30 minutes of signal averaging per curve — including realistic ms-duration photocapacitance "reset" delays — are shown in Fig. 6D. A photocapacitance risetime of $10 \pm 2\,\mathrm{ns}$ is clearly resolved.

The data of Figs. 5 and 6 highlight the special ability of pk-EFM to measure fast photocapacitance signals. Another advantage of the pk-EFM experiment is that, in contrast with tr-EFM, time resolution during evolution and sensitivity during detection can be separately optimized. This advantage is explained in Fig. 7. The tr-EFM experiment measures the photocapacitance risetime constant *directly* by demodulating the cantilever oscillation *versus* time data using a lock-in amplifier filter with bandwidth b_L and fitting the resulting frequency shift *versus* time data. The lock-in filter bandwidth limits the time resolution of the measurement since the measured frequency shift convolves the cantilever frequency shift with the lock-in's filter function (Fig. 7A and B). The wide filter bandwidth necessary to obtain improved time resolution also

increases noise, as shown in Fig. 7B and Fig. 1C. Any such *direct* measurement faces the same trade-off: detector bandwidth b_{L} determines the time resolution $t_{\mathrm{r}} = 1/2\pi b_{\mathrm{L}}$; increasing b_{L} to reduce t_{r} leads to a larger mean-square frequency noise.

In contrast, pk-EFM is sensitive to arbitrarily fast changes in photocapacitance during the pulse time t_{p}. Time resolution is obtained by using short pulse times t_{p}. The ultimate time resolution is limited only by the ability to modulate the tip voltage, which can be as fast as picoseconds (*45–47*). We are free to employ a phase filter to minimize the effect of surface and detection noise (Fig. 7D; Supplementary texts 2 and 3). Figure 7E plots the power spectrum of the filtered phase fluctuations. The Fig. 7D filter successfully rejects both low frequency surface-induced noise and high frequency detector noise. The Fig. 7D filter — and therefore the mean-square phase noise — is essentially independent of the pulse time t_{p} for short pulse times.

Discussion

In this work, we demonstrate a new indirect photocapacitance measurement, pk-EFM. The pk-EFM measurement uses the cantilever as a mechanical integrator and measures cantilever phase shift, a new observable. By measuring phase shift, the average frequency shift during the pulse is inferred without relying on slow modulation and lock-in techniques.

A comparison with the tr-EFM experiment is instructive. In FF-trEFM the cantilever oscillation is detected, demodulated, and filtered; the measured parameter is the time t_{FP} at which the resulting cantilever frequency transient reaches a maximum. This empirical calibration step reduces the entire photocapacitance transient to a single number, t_{FP}. This observed quantity depends not just on the photocapacitance risetime but on a number of ancillary parameters including the filter parameters and the sample's steady-state photocapacitance. For this reason, an empirical calibration step is required to relate the measured t_{FP} to the sample's underlying

photocapacitance risetime. It is unclear how this calibration procedure works if the sample's photocapacitance evolves on multiple time scales, as does the sample studied here. The time resolution of the tr-EFM measurement is limited by the detector bandwidth.

In pk-EFM the cantilever charge is pulsed and the cantilever oscillation is detected, modulated, and filtered; the measured parameter is the cantilever phase shift. Like ultrafast STM and KPFM photovoltage measurements, pk-EFM is an *indirect* measurement. Indirect measurements record only the *average* detector signal. To build up a picture of the sample's fast dynamics, the average detector signal is measured for a series of different time-offset electrical or optical pulses. The time resolution is limited only by the duration or jitter of the pulses. Crucially, indirect measurements require a system non-linearity so that the average detector signal responds to changes in pulse length, delay, or frequency. The phase shift $\Delta\phi$ in the pk-EFM experiment depends on the product of C_{t}'' and V_{t}, so the limited-duration tip-voltage pulses provide the necessary non-linearity.

In the pk-EFM experiment, no calibration step is required and the full photocapacitance transient is recovered by measuring the phase shift as a function of the pulse time. In contrast to previous indirect KPFM measurements, pk-EFM makes one phase shift measurement per pulse time, providing crucially important flexibility to include arbitrary wait times and voltage pulses before or after each measurement. This experimental flexibility allows pk-EFM to obtain reproducible photocapacitance measurements in organic semiconductor samples despite lengthy charge equilibration times.

The indirect nature of the pk-EFM method allows it to measure the full photocapacitance transient, not just the photocapacitance risetime. This capability was demonstrated here by uncovering a second, fast photocapacitance risetime not observed before in a nominally well-studied material. The pk-EFM measurement employs well-defined cantilever physics, which enables simulation (including relevant noise sources) of the experiment across a range of timescales.

The experiment admits a rigorous signal-to-noise analysis which details how sample fluctuations, thermal noise, and detection noise affect the measurement's phase resolution. The experiments show that pk-EFM is capable of measuring a photocapacitance transient whose risetime is much shorter than the inverse demodulation bandwidth and the cantilever period. Numerical simulations indicate that pk-EFM is capable of resolving a photocapacitance transient whose dynamics are six orders of magnitude faster than the inverse detection bandwidth (Fig. 6G).

The pk-EFM measurement, with a faster pulsed light source and modest improvements in the time response of the cantilever-circuit charging time, is poised to achieve nanosecond resolution, comparable to what time-resolved microwave conductivity can achieve. Nanosecond-resolution TRMC measurements have generated the first evidence that Marcus theory governs charge carrier generation in dilute donor-acceptor films prepared on non-conductive substrates (*24*). TRMC measures the charge-mobility product. Despite Ginger *et al.*'s empirical connection between the tr-EFM risetime and device efficiency, it is not yet clear what microscopic material property the time-resolved EFM photocapacitance experiment is measuring. Ginger and coworkers observe that light affects primarily the risetime, not the magnitude, of the photocapacitance signal in the EFM experiment. This finding suggests to us that the tr-EFM experiment is mainly probing the sample's photoconductivity. More work is required to test this hypothesis. Tirmzi *et al.* recently reformulated a theory for the EFM experiment that explicitly incorporates the complex sample impedance (*48*). Unifying this improved treatment of the EFM experiment with the pk-EFM theory presented here should allow us to connect the pk-EFM transient signal to materials properties and, ultimately, to microscopic theory.

Given its high temporal and spatial resolution, the phase-kick electric force microscope method introduced here clearly opens up many exciting possibilities for studying charge carrier generation and recombination in a wide range of device-relevant semiconductor films.

Supplementary Material accompanies this paper at `http://www.scienceadvances.org/`.

Materials and Methods

Sample preparation

ITO substrates (Nanocs, $10\,\Omega/\text{sq.}$) for depositing organic semiconductors were scrubbed with an Aquet liquid detergent/DI water solution, rinsed with DI water, and sonicated in a fresh Aquet solution for five minutes. The chips were rinsed, sonicated in pure DI water for five minutes and dried with high pressure nitrogen gas. Prior to depositing the solar cell blend, the chips were plasma cleaned for 10 minutes.

To prepare organic bulk heterojunction samples, $75\,\text{mg}$ of PFB (poly(9,9'-dioctylfluorene-*co*-bis-*N,N'*-(4-butylphenyl)-bis-*N,N'*-phenyl-1,4-phenylenediamine)) and F8BT (poly(9,9'-dioctylfluorene-*co*-benzothiadiazole)) were separately dissolved in $5\,\text{mL}$ p-xylenes. The solutions were filtered using PTFE syringe filters, then mixed together and used immediately. Approximately $200\,\mu\text{L}$ was deposited on an indium tin oxide (ITO) substrate and was spin coated at 2000 rpm for $60\,\text{s}$. All sample preparation was done in a dark room under orange light, and samples were immediately transferred to a nitrogen glovebox. The samples were transferred from the glovebox to the microscope at night, under red light illumination, and exposed to air for less than 15 minutes.

Scanned probe microscopy

All experiments were performed under vacuum ($8 \times 10^{-7}\,\text{mbar}$) in a custom-built scanning Kelvin probe microscope (*49*). The cantilever (MikroMasch HQ:NSC18/Pt conductive probe) had resonance frequency $f = 62.000\,\text{kHz}$, spring constant $k = 6.9\,\text{N}\,\text{m}^{-1}$ and quality factor

$Q = 28000$ (Supplementary text 11 and Fig. S9). Cantilever motion was detected using a fiber interferometer operating at 1490 nm (Corning SMF-28 fiber). The laser diode's (QPhotonics laser diode QFLD1490-1490-5S) DC current was set using a precision current source (ILX Lightwave LDX-3620) and the current was modulated at radiofrequencies using the input on the laser diode mount (ILX Lightwave LDM-4984, temperature controlled with ILX Lightwave LDT-5910B) (*50*). The interferometer light was detected with a $200\,\mathrm{kHz}$ bandwidth photodetector (New Focus model 2011, built-in high-pass filter set to $300\,\mathrm{Hz}$) and digitized at $1\,\mathrm{MHz}$ (National Instruments, PCI-6259). The cantilever was driven using a commercial phase locked loop (PLL) cantilever controller (RHK Technology, PLLPro2 Universal AFM controller), with PLL loop bandwidth $1.2\,\mathrm{kHz}$ (PLL feedback loop integral gain $I = 2.5\,\mathrm{Hz}^{-1}$, proportional gain $P = -12\,\mathrm{degrees/Hz}$).

For pk-EFM and tr-EFM photocapacitance measurements, the sample was illuminated from above with a fiber-coupled $405\,\mathrm{nm}$ laser (Thorlabs, LP405-SF10, held at $25\,^{\circ}\mathrm{C}$ with a Thorlabs TED200C). The laser was turned on and off using the external modulation input of the laser's current controller (Thorlabs, LDC202, $200\,\mathrm{kHz}$ bandwidth), and the laser power was measured using a fiber coupled power meter for each external voltage input. The light was coupled to the sample using a $50\,\mu\mathrm{m}$ core, 0.22 numerical aperture fiber (Thorlabs FG050LGA) (*49*). The estimated spot size on the sample was $(330 \times 120)\ \mu\mathrm{m}^2$, and the illumination intensity was estimated from the measured power and estimated spot size. The measured switching delay was $3.4\,\mu\mathrm{s}$, with a $2.5\,\mu\mathrm{s}$ 0 to 100 percent risetime (Fig. S11). The tip voltage was switched to $10\,\mathrm{V}$ beginning $50\,\mathrm{ms}$ before the start of the light pulse, in order to allow sample charges to equilibrate (Fig. 2D). The cantilever drive was switched off $10\,\mathrm{ms}$ before the start of the light pulse to avoid complicating the cantilever motion with artifacts from the PLL response (*7*). A commercial pulse and delay generator (Berkeley Nucleonics, BNC565) was used to generate tip voltage and light modulation pulses, as well as to turn off the cantilever drive voltage. The

BNC565 was triggered synchronous with the cantilever oscillation (Supplementary text 12). Between individual pulses, the sample was allowed to recover for $87\,\mathrm{ms}$ to $4\,\mathrm{s}$ with the tip voltage $V_\mathrm{t} = 0\,\mathrm{V}$.

Swept-voltage KPFM curves were taken before and after each pk-EFM or tr-EFM measurement to determine the tip-sample capacitance and surface potential (*51*). The sample's voltage (controlled with Keithley Model 2400) was adjusted to the sample's surface potential (typically 0.2 to $0.4\,\mathrm{V}$), so that $V_\mathrm{t} - \Phi$ was held constant. Measurements were performed $250 \pm 10\,\mathrm{nm}$ above the surface, determined by measuring the 50 percent amplitude reduction point before and after each measurement. Datasets with significant tip-sample drift ($> 10\,\mathrm{nm}$) over the course of the 1 to 20 minute measurement were discarded. The initial cantilever zero-to-peak amplitude was $A = 50\,\mathrm{nm}$. At $t = 0$ the cantilever zero-to-peak amplitude was $42\,\mathrm{nm}$.

The raw cantilever oscillation data (digitized at $1\,\mathrm{MHz}$) was saved along with counter timings (PCI-6259, 80 MHz counter) indicating the precise starting time of the light pulse (synchronized to the cantilever oscillation), allowing the start of the the light pulse to be determined to within $12.5\,\mathrm{ns}$. Along with each pk-EFM phase shift data point, a control data point, identical except without turning on the light, was collected.

Data workup

The data was processed in Python using a virtual lock-in amplifier technique. First, the data was processed through a fixed-frequency lock-in amplifier, with the reference frequency f_ref equal to the frequency where the data's Fourier transform was a maximum. The lock-in filter was a modified Blackman finite impulse response filter, as described in Supporting Discussion 2, designed to pass frequencies below $f_\mathrm{LP1} = 2\,\mathrm{kHz}$ and to eliminate frequencies above $f_\mathrm{LP2} = 8\,\mathrm{kHz}$ (3 dB bandwidth $3.84\,\mathrm{kHz}$). To precisely determine the additional light-induced phase shift in the vicinity of large changes to the cantilever frequency caused by stepping the cantilever

tip voltage, the data was also processed with a *frequency-variable* virtual lock-in amplifier, with

$$f_{\mathrm{ref}} = \begin{cases} f_1 & t \leq t_{\mathrm{p}} \\ f_2 & t > t_{\mathrm{p}}. \end{cases} \tag{31}$$

The complex output z of the lock-in amplifier was demodulated into amplitude $A = |z|$ and phase $\phi = \arg z$. The frequency was calculated from the phase using a central-difference numerical derivative.

pk-EFM phase difference filter The filtering of the frequency and phase was performed analogously. The frequency f_1 was chosen to be the best estimate of the cantilever frequency before the start of the light pulse, determined by averaging $f(t)$ out of the lock-in with an exponential weighting with a time constant of $0.67\,\mathrm{ms}$. The frequency f_2 was chosen to be the best estimate of the cantilever frequency after the end of the voltage pulse, using a $1.2\,\mathrm{ms}$ exponential time constant. These same time constants were used to determine the phase estimate of the cantilever phase before and after the pulse. The time constants were chosen to minimize the noise, which is determined by the competition between low-frequency surface-induced noise, which needs to be allowed through the filter to better estimate the *actual* frequency and phase, and high-frequency detection noise, which needs to be rejected to estimate frequency and phase as precisely as possible. The time constants are different because after the pulse the tip voltage was set to $V_{\mathrm{t}} = 0\,\mathrm{V}$, reducing the surface noise and allowing the phase and frequency to be determined more precisely by averaging for a longer time (Fig. S3). The phase before and after the pulse was determined using a weighted linear fit with the same exponential weighting used to determine the frequency (Supplementary text 3). The phase difference filter is shown in Fig. 7D.

As illustrated in Fig. 7D and Supplementary Fig. S4, a weighted linear fit, with the same exponential time constants used to determine f_1, f_2, was use to analyze the control data before and after the end of the pulse. To determine the precise cantilever phase at the end of the pulse,

the 20 displacement data points nearest to $t = t_{\mathrm{p}}$ were used to create a Krogh interpolator in Scipy (*52, 53*). The Krogh interpolator and its first derivative evaluated at t_{p} give the cantilever position x and velocity v. The cantilever phase was calculated from x and v using,

$$\phi|_{t=t_{\mathrm{p}}} = \arg(x - \frac{v}{2\pi f[k]}i) \tag{32}$$

$$t_{\mathrm{d}} = 2\pi\phi f[k], \tag{33}$$

where $f[k]$ is the cantilever frequency determined by the digital lock-in amplifier at the data point nearest in time to t_{p}.

The resulting amplitude change ΔA *vs*. delay time t_{d} and phase shift $\Delta\phi$ *versus* t_{d} plots were fit to sinusoids, and the best-fit phase shift was used to correct the raw phase shift data acquired in the light-on pk-EFM dataset (Fig. 4A). The corrected phase shifts are plotted in Fig. 4(A and C).

The tr-EFM data was processed with a filter bandwidth dependent on the fastest time constant in the sample ($f_{\mathrm{LP1}} = 4\,\mathrm{kHz}$, $f_{\mathrm{LP2}} = 15\,\mathrm{kHz}$ for the $20, 100\,\mathrm{kW\,m^{-2}}$ intensity data sets). The resulting frequency-*versus*-time data was aligned relative to the start of the light pulse and averaged ($N = 32$ to 384). The $100\,\mathrm{kW\,m^{-2}}$ tr-EFM data is shown in Fig. 7B. See Supplementary text 2 for more information.

Statistical analysis

Signal-averaged tr-EFM frequency shift *versus* time data and processed phase shift *versus* pulse time data was fit to bi-exponentials using PyStan (*54*), a programming environment for Bayesian modeling. In both cases, the data was modeled assuming that the frequency shift *versus* time data was constant before the light pulse, and was characterized by a bi-exponential decay afterwards. The tr-EFM average frequency $\bar{f}$ and standard error σ_f at each time t were used to model the experimental data. The mean frequency shift $\bar{f}$ was modeled as normally distributed

with standard deviation equal to the standard error. Using the notation $y \sim \mathcal{N}(\mu, \sigma)$ to indicate y is distributed normally ($\mathcal{N}$) with mean μ and standard deviation σ, the tr-EFM model was

$$\begin{cases} \bar{f}[t] \sim \mathcal{N}(f_0, \sigma_f[t]) & t \leq 0 \\ \bar{f}[t] \sim \mathcal{N}(f_0 + \Delta f_\infty \left[r(1 - e^{-t/\tau_1}) + \right. & \\ \qquad \left. (1-r)(1 - e^{-t/\tau_2}) \right], \sigma_f[t]) & t > 0, \end{cases} \tag{34}$$

where $\bar{f}[t], \sigma_f[t]$ were the experimental mean frequency shift and standard error calculated from signal-averaging N tr-EFM measurements. The model's parameters were f_0, the cantilever frequency before the pulse; Δf_∞, the steady state frequency shift caused by the photocapacitance; r, the fraction of the steady state frequency shift attributed to the faster time constant; and τ_1 and τ_2, the exponential time constants, with $\tau_1 < \tau_2$.

The pk-EFM model was more complicated, because more low-frequency phase noise enters the measurement at longer pulse times. We captured this time-dependent phase noise by modeling the phase noise standard deviation $\sigma_\phi[t_\mathrm{p}]$ as

$$\sigma_\phi[t_\mathrm{p}] = \sigma_0 + \sigma_1 t_\mathrm{p} + \sigma_2 t_\mathrm{p}^2, \tag{35}$$

with σ_0, σ_1, and σ_2 parameters. We modeled the observed $\Delta\phi[t_\mathrm{p}]$ using

$$\mu_\phi[t_\mathrm{p}] = \Delta f_\infty \left[r \left\{ t_\mathrm{p} - \tau_1 + \tau_1 e^{-t_\mathrm{p}/\tau_1} \right\} + \right. \tag{36}$$
$$\left. (1-r) \left\{ t_\mathrm{p} - \tau_2 + \tau_2 e^{-t_\mathrm{p}/\tau_2} \right\} \right]$$
$$\phi[t_\mathrm{p}] \sim \mathcal{N}(\mu_\phi[t_\mathrm{p}], \sigma_\phi[t_\mathrm{p}]), \tag{37}$$

where $\mu_\phi[t_\mathrm{p}]$ is the integral of the frequency shift induced by the light pulse (Eqs. 3 and 19).

For both models, weakly informative priors were chosen for $\Delta f_\infty, \tau_1$, and τ_2. A uniform prior between 0 and 1 was used for the ratio r. Noise parameters σ_0, σ_1, and σ_2 used implicit flat priors. The parameter means, standard deviations, and 15, 50, 85 percentile best fit curves in Fig. 4 were calculated using at least $N = 6000$ samples drawn from the posterior. See Supplementary text 13 for more information.

References

1. R. Giridharagopal, G. Shao, C. Groves, D. S. Ginger, New SPM techniques for analyzing OPV materials. *Mater. Today* **13**, 50 – 56 (2010).

2. X.-D. Dang, *et al.*, Nanostructure and optoelectronic characterization of small molecule bulk heterojunction solar cells by photoconductive atomic force microscopy. *Adv. Funct. Mater.* **20**, 3314 – 3321 (2010).

3. J. R. O'Dea, L. M. Brown, N. Hoepker, J. A. Marohn, S. Sadewasser, Scanned probe microscopy of solar cells: From inorganic thin films to organic photovoltaics. *MRS Bull.* **37**, 642 – 650 (2012).

4. J. L. Luria, *et al.*, Spectroscopic imaging of photopotentials and photoinduced potential fluctuations in a bulk heterojunction solar cell film. *ACS Nano* **6**, 9392 – 9401 (2012).

5. E. J. Spadafora, R. Demadrille, B. Ratier, B. Grevin, Imaging the carrier photogeneration in nanoscale phase segregated organic heterojunctions by Kelvin probe force microscopy. *Nano Lett.* **10**, 3337 – 3342 (2010).

6. D. C. Coffey, D. S. Ginger, Time-resolved electrostatic force microscopy of polymer solar cells. *Nat. Mater.* **5**, 735 – 740 (2006).

7. R. Giridharagopal, *et al.*, Submicrosecond time resolution atomic force microscopy for probing nanoscale dynamics. *Nano Lett.* **12**, 893 – 898 (2012).

8. P. A. Cox, *et al.*, Imaging charge transfer state excitations in polymer/fullerene solar cells with time-resolved electrostatic force microscopy. *J. Phys. Chem. Lett.* **6**, 2852 – 2858 (2015).

9. D. U. Karatay, J. S. Harrison, M. S. Glaz, R. Giridharagopal, D. S. Ginger, Fast time-resolved electrostatic force microscopy: Achieving sub-cycle time resolution. *Rev. Sci. Instrum.* **87**, 053702 (2016).

10. D. P. McMahon, D. L. Cheung, A. Troisi, Why holes and electrons separate so well in polymer/fullerene photovoltaic cells. *J. Phys. Chem. Lett.* **2**, 2737 – 2741 (2011).

11. A. A. Bakulin, *et al.*, The role of driving energy and delocalized states for charge separation in organic semiconductors. *Science* **335**, 1340 – 1344 (2012).

12. T. J. Savenije, A. J. Ferguson, N. Kopidakis, G. Rumbles, Revealing the dynamics of charge carriers in polymer:fullerene blends using photoinduced time-resolved microwave conductivity. *J. Phys. Chem. C* **117**, 24085 – 24103 (2013).

13. K. Vandewal, *et al.*, Efficient charge generation by relaxed charge-transfer states at organic interfaces. *Nat. Mater.* **13**, 63 – 68 (2013).

14. B. M. Savoie, N. E. Jackson, L. X. Chen, T. J. Marks, M. A. Ratner, Mesoscopic features of charge generation in organic semiconductors. *Acc. Chem. Res.* **47**, 3385 – 3394 (2014).

15. S. D. Dimitrov, J. R. Durrant, Materials design considerations for charge generation in organic solar cells. *Chem. Mater.* **26**, 616 – 630 (2014).

16. S. Albrecht, *et al.*, On the efficiency of charge transfer state splitting in polymer:fullerene solar cells. *Adv. Mater.* **26**, 2533 – 2539 (2014).

17. N. E. Jackson, B. M. Savoie, T. J. Marks, L. X. Chen, M. A. Ratner, The next breakthrough for organic photovoltaics? *J. Phys. Chem. Lett.* **6**, 77 – 84 (2015).

18. T. M. Burke, S. Sweetnam, K. Vandewal, M. D. McGehee, Beyond Langevin recombination: How equilibrium between free carriers and charge transfer states determines the open-circuit voltage of organic solar cells. *Adv. Energy Mater.* **5**, 1500123 (2015).

19. H. M. Feier, *et al.*, Local intermolecular order controls photoinduced charge separation at donor/acceptor interfaces in organic semiconductors. *Adv. Energy Mater.* **6**, 1502176 (2016).

20. M. Causá, *et al.*, The fate of electron–hole pairs in polymer:fullerene blends for organic photovoltaics. *Nat. Comms.* **7**, 12556 (2016).

21. B. W. Larson, *et al.*, Inter-fullerene electronic coupling controls the efficiency of photoinduced charge generation in organic bulk heterojunctions. *Adv. Energy Mater.* p. 1601427 (2016).

22. C. Deibel, A. Wagenpfahl, V. Dyakonov, Origin of reduced polaron recombination in organic semiconductor devices. *Phys. Rev. B* **80**, 075203 (2009).

23. A. J. Ferguson, N. Kopidakis, S. E. Shaheen, G. Rumbles, Dark carriers, trapping, and activation control of carrier recombination in neat P3HT and P3HT:PCBM blends. *J. Phys. Chem. C* **115**, 23134 – 23148 (2011).

24. D. C. Coffey, *et al.*, An optimal driving force for converting excitons into free carriers in excitonic solar cells. *J. Phys. Chem. C* **116**, 8916–8923 (2012).

25. R. J. Hamers, D. G. Cahill, Ultrafast time resolution in scanned probe microscopies. *Appl. Phys. Lett.* **57**, 2031 (1990).

26. S. Weiss, D. F. Ogletree, D. Botkin, M. Salmeron, D. S. Chemla, Ultrafast scanning probe microscopy. *Appl. Phys. Lett.* **63**, 2567 (1993).

27. G. Nunes, M. R. Freeman, Picosecond resolution in scanning tunneling microscopy. *Science* **262**, 1029–1032 (1993).

28. S. Grafström, Photoassisted scanning tunneling microscopy. *J. Appl. Phys.* **91**, 1717 (2002).

29. O. Takeuchi, R. Morita, M. Yamashita, H. Shigekawa, Development of time-resolved scanning tunneling microscopy in femtosecond range. *Jap. J. Appl. Phys.* **41**, 4994–4997 (2002).

30. O. Takeuchi, *et al.*, Probing subpicosecond dynamics using pulsed laser combined scanning tunneling microscopy. *Appl. Phys. Lett.* **85**, 3268 (2004).

31. T. L. Cocker, *et al.*, An ultrafast terahertz scanning tunnelling microscope. *Nat. Photon.* **7**, 620–625 (2013).

32. M. Eisele, *et al.*, Ultrafast multi-terahertz nano-spectroscopy with sub-cycle temporal resolution. *Nat. Photon.* **8**, 841–845 (2014).

33. M. Takihara, T. Takahashi, T. Ujihara, Minority carrier lifetime in polycrystalline silicon solar cells studied by photoassisted Kelvin probe force microscopy. *Appl. Phys. Lett.* **93**, 021902 (2008).

34. G. Shao, M. S. Glaz, F. Ma, H. Ju, D. S. Ginger, Intensity-modulated scanning Kelvin probe microscopy for probing recombination in organic photovoltaics. *ACS Nano* **8**, 10799–0807 (2014).

35. J. Murawski, *et al.*, Pump-probe Kelvin-probe force microscopy: Principle of operation and resolution limits. *J. Appl. Phys.* **118**, 154302 (2015).

36. J. Murawski, *et al.*, Tracking speed bumps in organic field-effect transistors via pump-probe Kelvin-probe force microscopy. *J. Appl. Phys.* **118**, 244502 (2015).

37. Z. Schumacher, Y. Miyahara, A. Spielhofer, P. Grutter, Measurement of surface photovoltage by atomic force microscopy under pulsed illumination. *Phys. Rev. Appl.* **5**, 044018 (2016).

38. D. Coffey, Characterizing the local optoelectronic performance of organic solar cells with scanning-probe microscopy, Ph.D. thesis, University of Washington (2007).

39. W. Magnus, On the exponential solution of differential equations for a linear operator. *Comm. Pure Appl. Math.* **7**, 649 – 673 (1954).

40. S. Blanes, F. Casas, J. Oteo, J. Ros, The Magnus expansion and some of its applications. *Phys. Rep.* **470**, 151–238 (2009).

41. S. Kuehn, R. Loring, J. Marohn, Dielectric fluctuations and the origins of noncontact friction. *Phys. Rev. Lett.* **96**, 156103 (2006).

42. S. Yazdanian, J. Marohn, R. Loring, Dielectric fluctuations in force microscopy: Noncontact friction and frequency jitter. *J. Chem. Phys.* **128**, 224706 (2008).

43. N. Hoepker, S. Lekkala, R. F. Loring, J. A. Marohn, Dielectric fluctuations over polymer films detected using an atomic force microscope. *J. Phys. Chem. B* **115**, 14493-14500 (2011).

44. J. L. Hutter, J. Bechhoefer, Calibration of atomic-force microscope tips. *Rev. Sci. Instrum.* **64**, 1868 – 1873 (1993).

45. A. Hou, F. Ho, D. Bloom, Picosecond electrical sampling using a scanning force microscope. *Electron. Lett.* **28**, 2302 – 2303 (1992).

46. A. Leyk, C. Böhm, D. van der Weide, E. Kubalek, 104 GHz signals measured by high frequency scanning force microscope test systems. *Electron. Lett.* **31**, 1046 – 1047 (1995).

47. B. T. Rosner, D. W. van der Weide, High-frequency near-field microscopy. *Rev. Sci. Instrum.* **73**, 2505 (2002).

48. A. M. Tirmzi, R. P. Dwyer, T. Hanrath, J. A. Marohn, Coupled slow and fast charge dynamics in cesium lead bromide perovskite. *ACS Energy Lett.* **2**, 488 – 496 (2017).

49. J. L. Luria, Spectroscopic characterization of charge generation and trapping in third-generation solar cell materials using wavelength- and time-resolved electric force microscopy, Ph.D. thesis, Cornell University (2011).

50. D. Rugar, H. Mamin, P. Guethner, Improved fiber-optic interferometer for atomic force microscopy. *Appl. Phys. Lett.* **55**, 2588 – 2590 (1989).

51. L. M. Smieska, *et al.*, Following chemical charge trapping in pentacene thin films by selective impurity doping and wavelength-resolved electric force microscopy. *Adv. Funct. Mater.* **22**, 5096 – 5106 (2012).

52. E. Jones, T. Oliphant, P. Peterson, *et al.*, SciPy: Open source scientific tools for Python (2001–). [Online; accessed 2016-03-12].

53. F. T. Krogh, Efficient algorithms for polynomial interpolation and numerical differentiation. *Math. Comp.* **24**, 185–190 (1970).

54. S. D. Team, Pystan: the Python interface to Stan, version 2.8.0 (2015).

55. R. P. Dwyer, S. R. Nathan, J. A. Marohn, Data and workup for "Microsecond photocapacitance transients observed using a charged microcantilever as a gated mechanical integrator.", Available from http://github.com/ryanpdwyer/1605-phasekick (2016).

56. R. P. Dwyer, J. A. Marohn, The FreqDemod 0.2.1 Python package, Available for installation at https://pypi.python.org/pypi/FreqDemod. Documenta-

tion available at http://freqdemod.readthedocs.org. Source code available at https://github.com/JohnMarohn/FreqDemod. (2015).

57. C. Turner, Slope filtering: An FIR approach to linear regression. *IEEE Signal Process. Mag.* **25**, 159–163 (2008).

58. D. G. Cahill, Analysis of heat flow in layered structures for time-domain thermoreflectance. *Rev. Sci. Instrum.* **75**, 5119–5122 (2004).

59. J. Luria, *et al.*, Charge transport in CdTe solar cells revealed by conductive tomographic atomic force microscopy. *Nat. Energy* **1**, 16150 (2016).

60. A. Gelman, D. B. Rubin, Inference from iterative simulation using multiple sequences. *Statist. Sci.* **7**, 457–472 (1992).

61. M. Waskom, *et al.*, seaborn: v0.7.0 (2016).

Acknowledgements: The authors thank Dr. Brandon Wenning for assistance with sample preparation. **Funding:** The authors acknowledge support from Cornell University and the U.S. National Science Foundation (Grant DMR-1309540 and a Graduate Research Fellowship to S.R.N.). **Author contributions:** S.R.N. and R.P.D. and J.A.M. designed the experiments. R.P.D. performed the experiments, data analysis, and simulations. R.P.D. and J.A.M. wrote the paper. **Competing interests:** The authors declare that they have no competing interests. **Data and materials availability:** Experimental data and code to reproduce the analysis performed in this paper are available freely online (*55*). A standalone Python package for cantilever frequency demodulation is also available freely online (*56*). Additional data related to this paper may be requested from the authors.

Fig. 1. Experimental overview. (**A**) The experimental setup and sample, a spin-coated PFB:F8BT film on indium tin oxide. (**B**) The cantilever frequency shift δf depends parabolically on the tip voltage V_t. The increased curvature of the δf *vs.* V_t parabola under illumination indicates a light-induced increase in tip-sample capacitance. (**C**) Photocapacitance charging measured via the cantilever frequency and phase. Data demodulated with 3 dB bandwidth of $1.92\,\mathrm{kHz}$ (blue) and $0.96\,\mathrm{kHz}$ (purple). (**D**) When the light is turned off, but the voltage is still on, light-induced capacitance remains elevated for tens of seconds to minutes. The dashed line shows the frequency shift before the start of the light pulse. Average of 100 traces shown, each demodulated with 3 dB bandwidth $1.92\,\mathrm{kHz}$. Experimental parameters: tip-sample distance $h = 250\,\mathrm{nm}$; tip-sample voltage $V_\mathrm{t} = 10\,\mathrm{V}$; light intensity $I_{h\nu} = 0.1\,\mathrm{kW\,m^{-2}}$ in (C) and $I_{h\nu} = 20\,\mathrm{kW\,m^{-2}}$ in (D); light pulse time $50\,\mathrm{ms}$ in (C), $2.5\,\mathrm{ms}$ in (D).

Fig. 2. Using the pk-EFM experiment to measure a photocapacitance transient. For three representative pulse times, we plot (**A**) cantilever amplitude; (**B**) cantilever drive voltage, turned off at $t = -10\,\mathrm{ms}$; (**C**) tip voltage, with the pulse time t_p indicated; (**D**) sample illumination intensity, turned on at $t = 0$; (**E**) sample capacitance; and (**F**) cantilever frequency shift. (**G**) Timing of applied voltages and light pulses. The voltage and light turn off simultaneously at $t = t_\mathrm{p}$. After a delay t_d (typically 5 to $15\,\mathrm{ms}$), the cantilever drive voltage is turned back on. Next we illustrate how the phase shift $\Delta\phi$ is calculated using the $t_\mathrm{p} = 10.3\,\mathrm{ms}$ data. We process the cantilever displacement data using a software lock-in amplifier. (**H**) The software lock-in amplifier reference frequency changes at $t = t_\mathrm{p}$. The software lock-in amplifier outputs (**I**) the in-phase (solid), and out-of-phase (dashed) components of the cantilever displacement; (**J**) cantilever amplitude; (**K**) frequency shift; and (**L**) phase shift. The total phase shift $\Delta\phi$ is equal to the highlighted area under the cantilever frequency shift curve. (**M**) The voltage- and light-induced phase shift $\Delta\phi$ is measured as a function of the pulse time t_p. We show only every other data point for clarity. The $t_\mathrm{p} = 10.3\,\mathrm{ms}$ data point is denoted with a star. Experimental

parameters: PFB:F8BT-on-ITO film, $h = 250\,\mathrm{nm}$, $V_\mathrm{t} = 10\,\mathrm{V}$, $I_{h\nu} = 0.3\,\mathrm{kW\,m^{-2}}$, delay time between pulses = $1.5\,\mathrm{s}$.

Fig. 3. Phase space and lock-in detector representation of the pk-EFM experiment. Top: Sinusoidal cantilever displacement "signal" and square-wave "reference" oscillations versus time, initially (left), under illumination (middle), and with the illumination removed (right). Bottom: Evolution of the signal and reference oscillator as viewed in phase space (X = position, Y = momentum) and at the outputs of a lock-in detector (X_LI = in-phase channel, Y_LI = out-of-phase channel), at short time (middle) and at long time (right).

Fig. 4. Comparison of pk-EFM and tr-EFM signals (PFB:F8BT on ITO, $h = 250\,\mathrm{nm}$, and $V_\mathrm{t} = 10\,\mathrm{V}$). (**A**) pk-EFM phase shift *versus* pulse time data, collected at $100\,\mathrm{kW\,m^{-2}}$ intensity, overlaid with best-fit pk-EFM and tr-EFM phase shift curves. The control dataset (green) shows the observed phase shift with the light off. The gray points show the control data before correcting for the phase shift caused by the abrupt change in tip-sample voltage at the end of the pulse. (**B**) tr-EFM frequency shift *versus* time data, overlaid with best-fit tr-EFM and pk-EFM frequency shift curves. (**C**) Phase shift data collected across a range of light intensities. The photocapacitance transient rises more quickly at higher light intensities. Solid curves are a biexponential fit. The delay time between pulses was at least $87\,\mathrm{ms}$. (**D**) Time constants for biexponential fits of photocapacitance transients measured using pk-EFM and tr-EFM show a consistent trend.

Fig. 5. Direct measurements are insensitive to fast sample dynamics. Inferring the charging time *via* the cantilever frequency and phase (PFB:F8BT on ITO, $h = 250\,\mathrm{nm}$, $V_\mathrm{t} = 10\,\mathrm{V}$). (**A**) Cantilever tip voltage; (**B**) sample response function, with charging time constant τ_c; (**C**) lock-in amplifier response function; (**D**) measured cantilever amplitude with modeled, best-fit response for $\tau_\mathrm{c} = 0.1\,\mathrm{ns}$ (orange) and $\tau_\mathrm{c} = 1000\,\mathrm{ns}$ (purple) (**E**) Fit residuals: $0.1\,\mathrm{ns}$ orange circles, $1000\,\mathrm{ns}$ purple squares. (**F**) Measured cantilever frequency; and (**G**) measured cantilever phase.

Inferring the charging time directly from the cantilever displacement signal. (**H**) Cantilever tip voltage; (**I**) Sample response function; (**J**) Cantilever displacement, with best-fit sinusoid from the data before the voltage step ($t < 0$); (**K**) Change in cantilever displacement Δx_{V} induced by the voltage pulse, along with best-fit responses for $\tau_{\mathrm{c}} = 10\,\mathrm{ns}$ (orange) and $\tau_{\mathrm{c}} = 350\,\mathrm{ns}$ (purple). (**L**) Fit residuals: $10\,\mathrm{ns}$ orange circles, $350\,\mathrm{ns}$ purple squares.

Fig. 6. Experiments and simulations demonstrating subcycle time resolution in pk-EFM. (**A**) Subcycle voltage-pulse control experiment (PFB:F8BT on ITO, $h = 250\,\mathrm{nm}$). A voltage pulse of length t_{p} is applied to the cantilever tip (top) at a delay of t_{d} relative to the cantilever oscillation (middle) for 100 consecutive cantilever oscillations. (**B**) The pulses shift the cantilever amplitude by ΔA. (**C**) Measured frequency shift; and (**D**) phase shift, demodulated with 3 dB bandwidth $4.8\,\mathrm{kHz}$ (blue) and $1.5\,\mathrm{kHz}$ (green). (**E**) The amplitude shift ΔA *vs.* delay time t_{d} for three representative pulse lengths. (**F**) The normalized response $\Delta A_{\mathrm{max}}/t_{\mathrm{p}}$ obtained by fitting data in (E) shows the cantilever wiring attenuating the response at short pulse times. The gray line is a fit to a single-exponential cantilever charging transient. (**G**) Numerically simulated phase shift in microcycles *vs.* t_{p} for a sample with a photocapacitance charging time of $50\,\mathrm{ns}$ (blue), $10\,\mathrm{ns}$ (green), and $2\,\mathrm{ns}$ (red). Solid lines are a fit to a single-exponential risetime model. Simulations include detector noise, thermomechanical cantilever position fluctuations, and sample-related frequency noise at levels comparable to those observed in the experiments of Fig. 4 (Supplementary text 10). The simulated data assumed 1600 averages per point ($16\,\mathrm{s/pt} = 1600 \times (2\,\mathrm{ms\ acq./pt} + 8\,\mathrm{ms\ delay/pt})$; total acquisition time = 30 minutes).

Fig. 7. Frequency noise and phase noise in tr-EFM and pk-EFM. (**A**) Cantilever position-*versus*-time data is demodulated using a filter with varying bandwidths (Fig. S2). (**B**) top: Fourier transform of the filters in (A); middle: experimental power spectral density of frequency fluctuations (PFB:F8BT on ITO, $V_{\mathrm{t}} = 0\,\mathrm{V}$, $h = 250\,\mathrm{nm}$); bottom: product of top and middle traces, shaded to indicate that the mean-square frequency noise is the integral under

this curve. (**C**) The cantilever phase (calculated by demodulation) is filtered to estimate the phase difference $\Delta\phi$ acquired during the pulse. The filters during the *before* ($t < 0$) and *after* ($t > t_\mathrm{p}$) periods are weighted least squares filters, with exponential weight time constants before $\tau_\mathrm{b} = 0.67\,\mathrm{ms}$ and after $\tau_\mathrm{a} = 1.2\,\mathrm{ms}$ (see supplementary text 3). (**D**) top: Fourier transform of the filter function in (C); middle: experimental power spectral density of phase fluctuations (PFB:F8BT on ITO, $V_\mathrm{t} = 0\,\mathrm{V}$, $h = 250\,\mathrm{nm}$); bottom: product of top and middle traces, shaded to indicate that the mean-square phase noise is the integral under this curve.

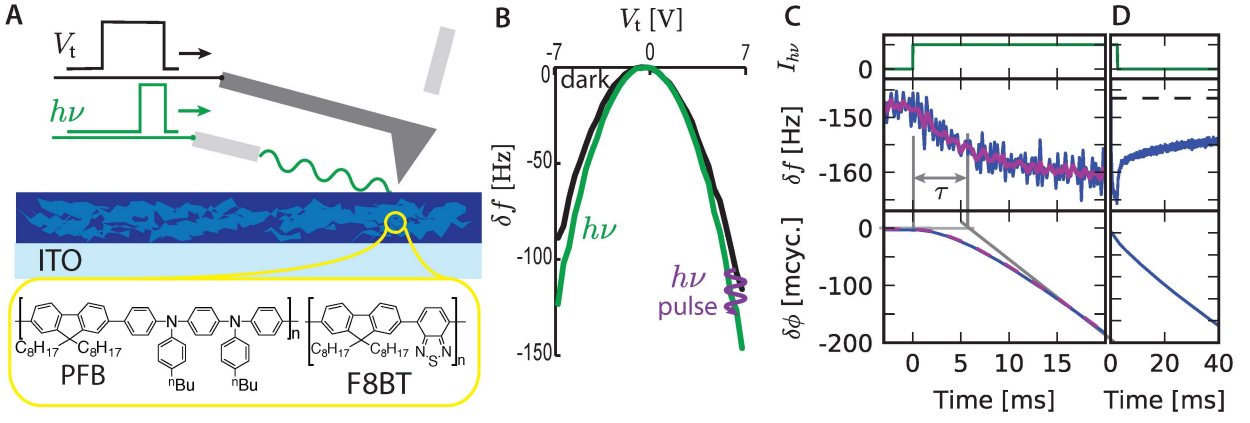
A
V_t
$h\nu$
ITO
PFB
F8BT
B
V_t [V]
-7
0
7
dark
$h\nu$
$h\nu$
pulse
δf [Hz]
0
-50
-100
-150
C
D
$I_{h\nu}$
δf [Hz]
$\delta\phi$ [mcyc.]
τ
0
-150
-160
-200
0
5
10
15
20
40
Time [ms]
Time [ms]

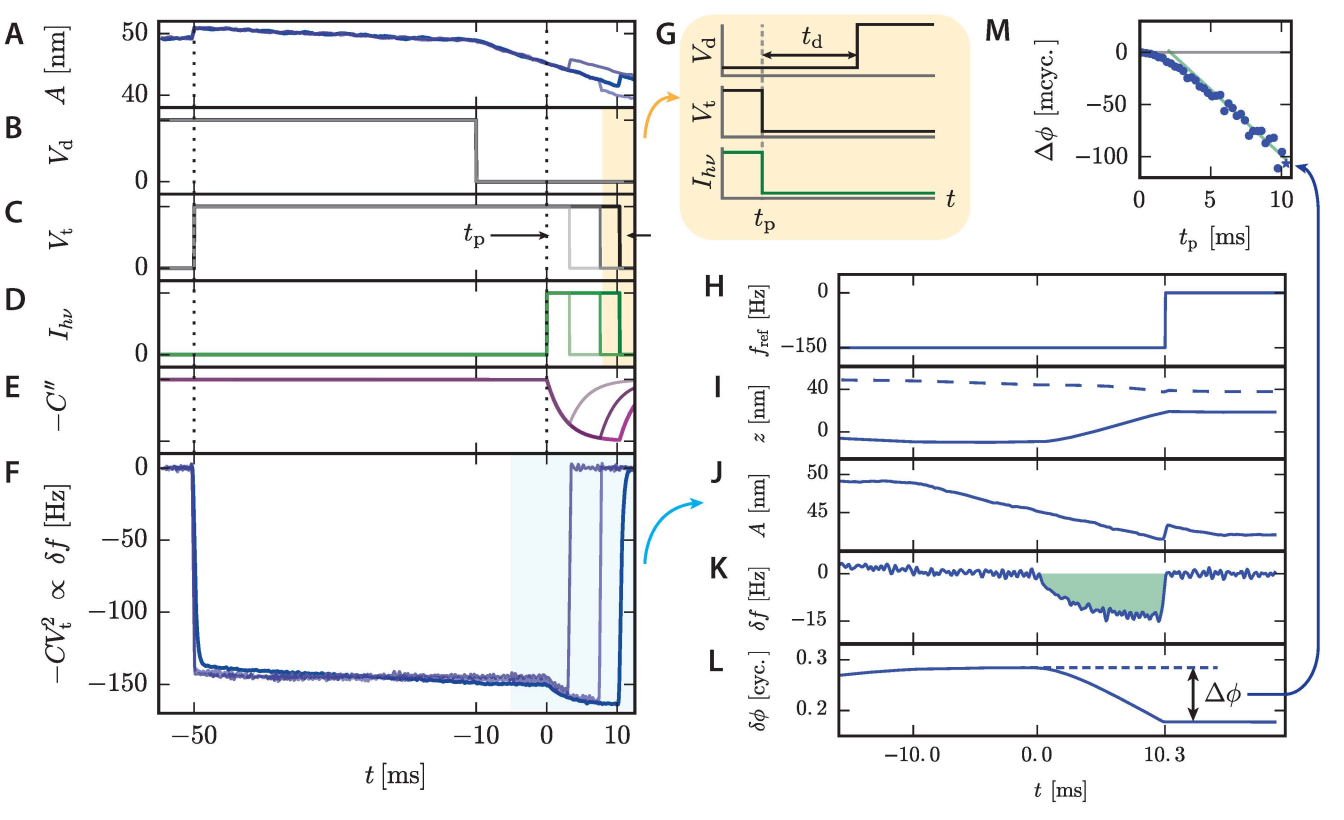
A
A [nm]
50
40
B
V_d
0
C
V_t
t_p
0
D
$I_{h\nu}$
0
E
$-C''$
F
$-CV_t^2 \propto \delta f$ [Hz]
0
−50
−100
−150
−50
−10
0
10
t [ms]
G
V_d
t_d
V_t
$I_{h\nu}$
t
t_p
M
$\Delta\phi$ [mcyc.]
0
−50
−100
0
5
10
t_p [ms]
H
f_{ref} [Hz]
0
−150
I
z [nm]
40
0
J
A [nm]
50
45
K
δf [Hz]
0
−15
L
$\delta\phi$ [cyc.]
0.3
0.2
$\Delta\phi$
−10.0
0.0
10.3
t [ms]

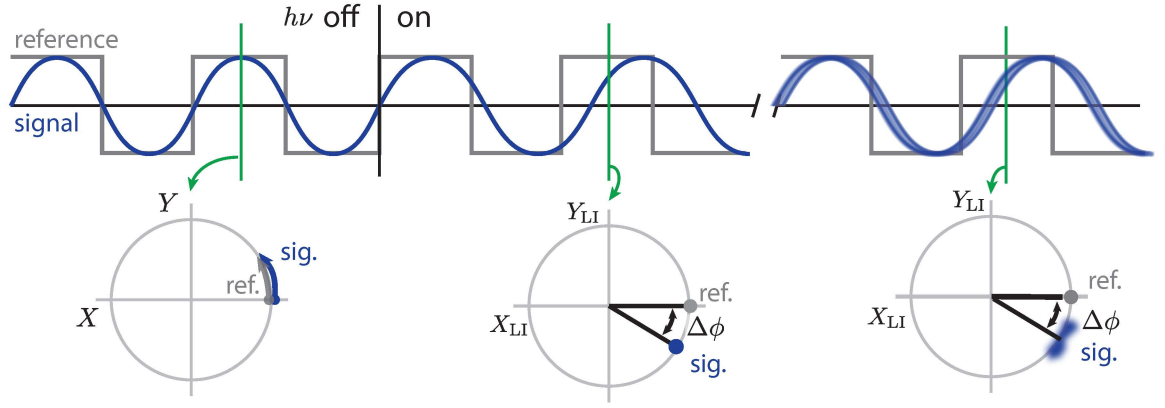
reference
signal
$h\nu$ off
on
Y
X
sig.
ref.
Y_{LI}
X_{LI}
ref.
$\Delta\phi$
sig.
Y_{LI}
X_{LI}
ref.
$\Delta\phi$
sig.

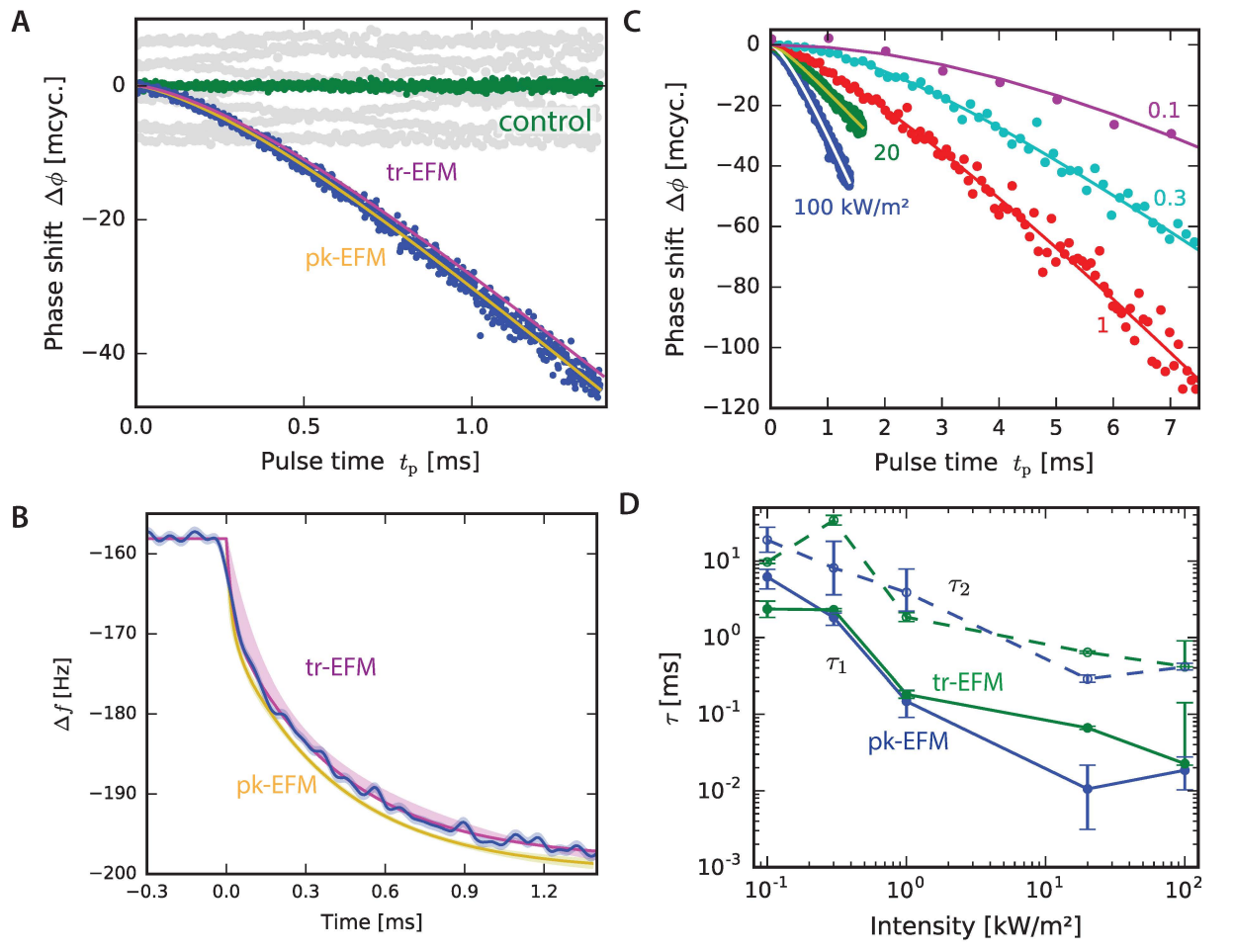
A
Phase shift Δφ [mcyc.]
0
−20
−40
0.0
0.5
1.0
Pulse time t_p [ms]
control
tr-EFM
pk-EFM
B
Δf [Hz]
−160
−170
−180
−190
−200
−0.3
0.0
0.3
0.6
0.9
1.2
Time [ms]
tr-EFM
pk-EFM
C
Phase shift Δφ [mcyc.]
0
−20
−40
−60
−80
−100
−120
0
1
2
3
4
5
6
7
Pulse time t_p [ms]
0.1
0.3
1
20
100 kW/m²
D
τ [ms]
10^1
10^0
10^{-1}
10^{-2}
10^{-3}
10^{-1}
10^0
10^1
10^2
Intensity [kW/m²]
τ_2
τ_1
tr-EFM
pk-EFM

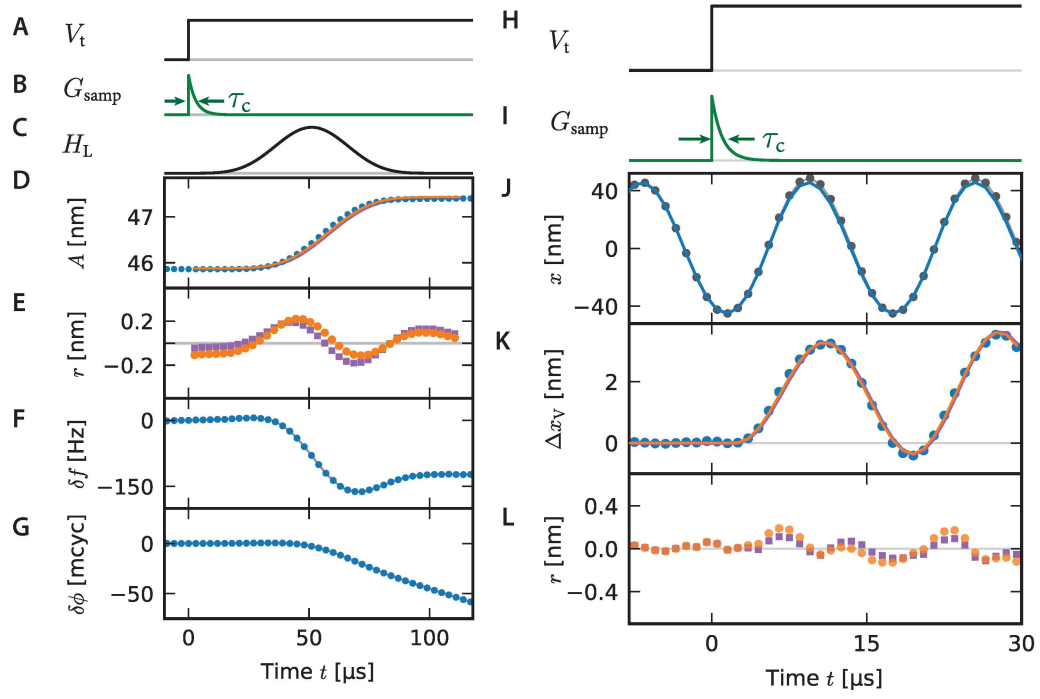
A
V_t
B
G_{samp}
τ_c
C
H_L
D
A [nm]
47
46
E
r [nm]
0.2
−0.2
F
δf [Hz]
0
−150
G
$\delta\phi$ [mcyc]
0
−50
0
50
100
Time t [μs]
H
V_t
I
G_{samp}
τ_c
J
x [nm]
40
0
−40
K
Δx_V [nm]
2
0
L
r [nm]
0.4
0.0
−0.4
0
15
30
Time t [μs]

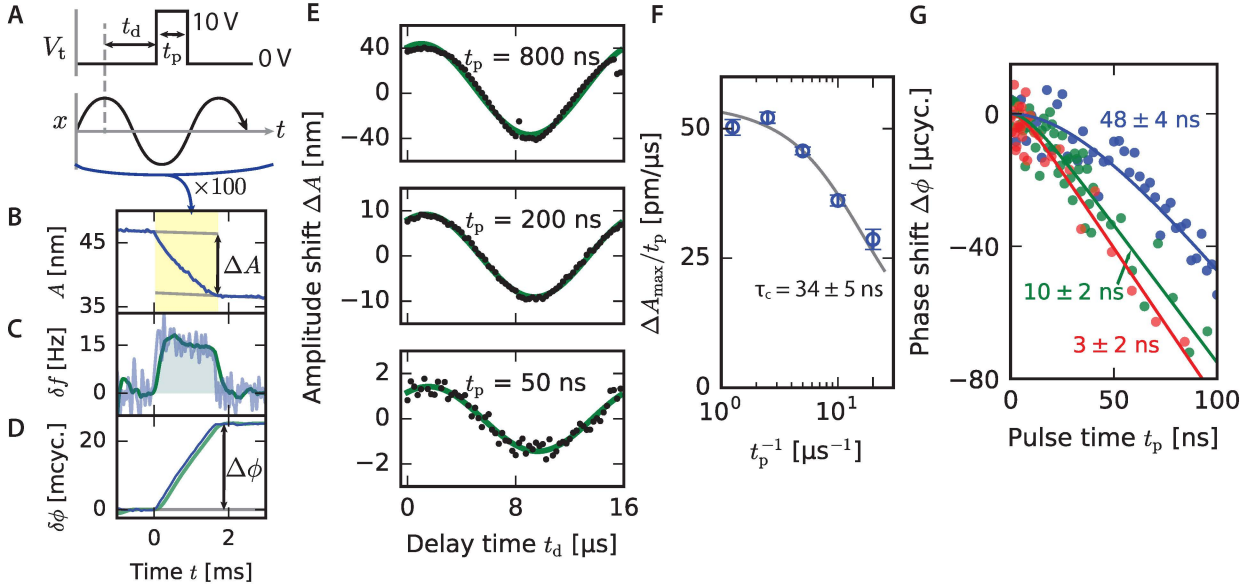
A
V_t
t_d
t_p
10 V
0 V
x
t
×100
B
45
35
A [nm]
ΔA
C
15
0
δf [Hz]
D
20
0
$\delta\phi$ [mcyc.]
$\Delta\phi$
0
2
Time t [ms]
E
t_p = 800 ns
t_p = 200 ns
t_p = 50 ns
Amplitude shift ΔA [nm]
Delay time t_d [µs]
F
$\Delta A_{max}/t_p$ [pm/µs]
$\tau_c = 34 \pm 5$ ns
t_p^{-1} [µs^{-1}]
G
Phase shift $\Delta\phi$ [µcyc.]
48 ± 4 ns
10 ± 2 ns
3 ± 2 ns
Pulse time t_p [ns]

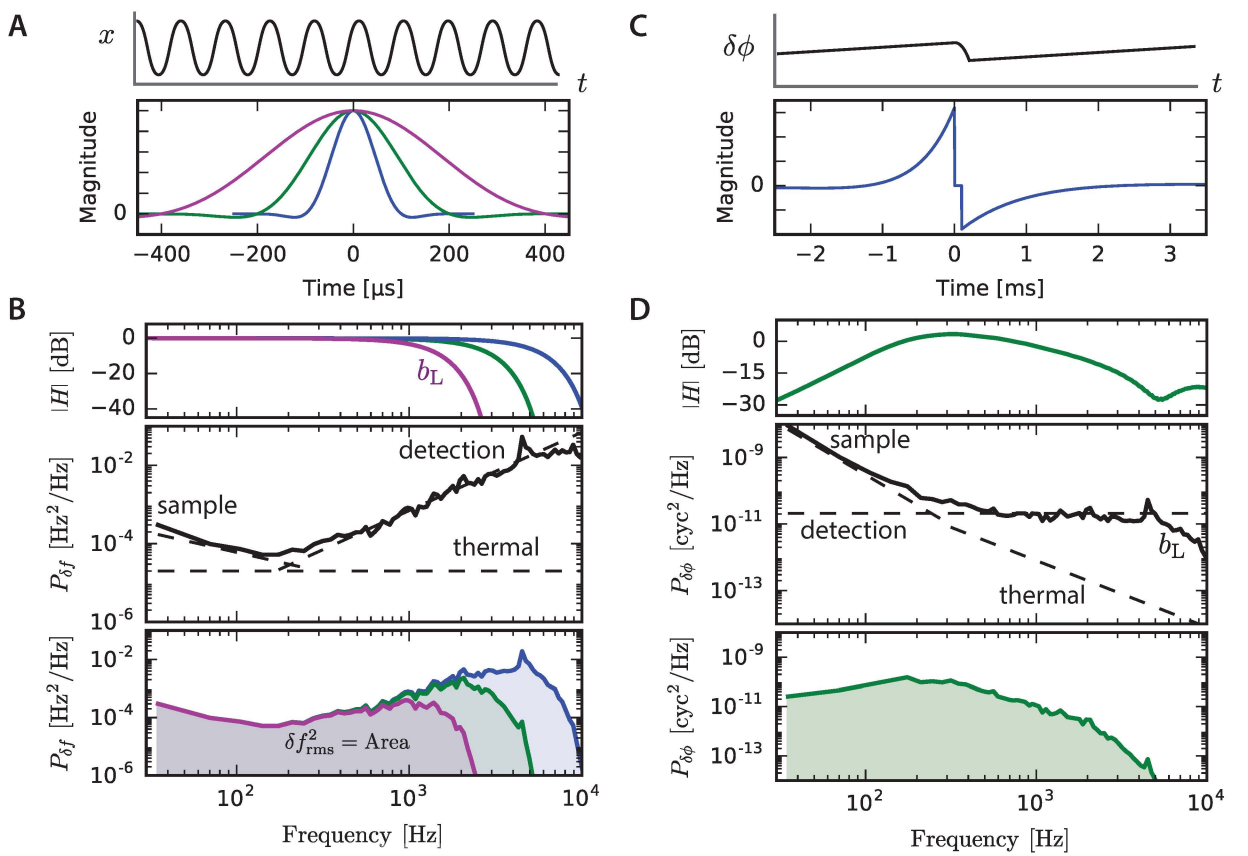
A
x
t
Magnitude
0
−400
−200
0
200
400
Time [μs]
C
δφ
t
Magnitude
0
−2
−1
0
1
2
3
Time [ms]
B
|H| [dB]
0
−20
−40
b_L
detection
sample
thermal
10^-2
10^-4
10^-6
P_δf [Hz^2/Hz]
δf^2_rms = Area
10^2
10^3
10^4
Frequency [Hz]
D
|H| [dB]
0
−15
−30
sample
detection
b_L
thermal
10^-9
10^-11
10^-13
P_δφ [cyc^2/Hz]
Frequency [Hz]

Supplemental Materials: Microsecond photocapacitance transients observed using a charged microcantilever as a gated mechanical integrator

Ryan P. Dwyer,[1] Sarah R. Nathan,[1] and John A. Marohn[1]

[1]*Department of Chemistry and Chemical Biology, Ithaca, New York 14853-1301*

(Dated: March 11, 2017)

This document contains:

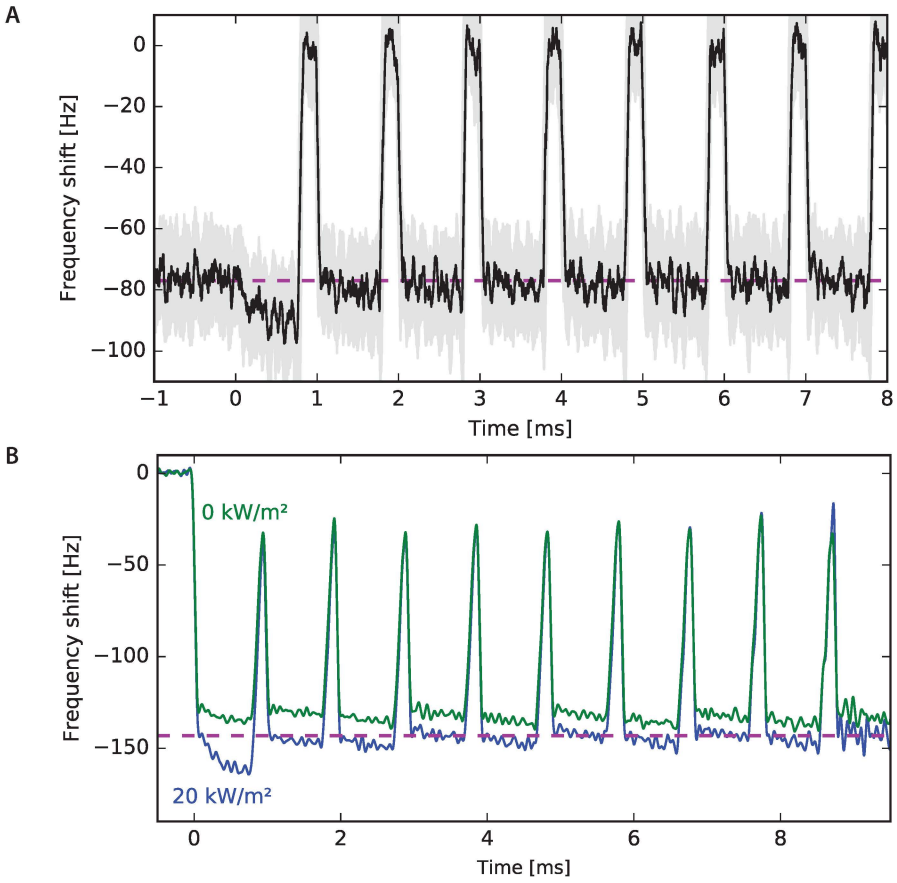

FIG. S1. **Fast clearing of remnant photocapacitance**. (**A**) At time $t = 0$ with the tip-sample voltage set to $V_\mathrm{t} = 7\,\mathrm{V}$, a light pulse was sent to the sample (PFB:F8BT on ITO, see Methods; pulse duration = $900\,\mu\mathrm{s}$; pulse intensity $I_{h\nu} = 20\,\mathrm{kW\,m^{-2}}$). Thereafter, the tip voltage was cycled to $0\,\mathrm{V}$ for $100\,\mu\mathrm{s}$ and to $7\,\mathrm{V}$ for $900\,\mu\mathrm{s}$. The dark line is the mean frequency shift for $N = 64$ averages, worked up using $f_{\mathrm{LP1}} = 4\,\mathrm{kHz}$, $f_{\mathrm{LP2}} = 15\,\mathrm{kHz}$ (see Fig. S2). The gray shaded region shows the 25th to 75th percentiles. The purple line shows the mean frequency shift before the pulse, and indicates that the photocapacitance has recovered after 1 or 2 pulses of $100\,\mu\mathrm{s}$ duration with $V_\mathrm{t} = 0$. (**B**) The same experiment is repeated with shorter duration waits at $0\,\mathrm{V}$. After the light pulse, the tip voltage is repeatedly cycled to $0\,\mathrm{V}$ for $8.5\,\mu\mathrm{s}$ and $7\,\mathrm{V}$ for $900\,\mu\mathrm{s}$.

S1. TIP VOLTAGE PHOTOCAPACITANCE CLEARING

Figure 1D shows that with the light off and the tip voltage V_t far from the the surface potential ϕ, the photocapacitance decays very slowly. By turning off the light and pulsing the tip voltage from $10\,\mathrm{V}$ back to $0\,\mathrm{V}$, we show that remnant photocapacitance can be cleared in 10s to 100s of microseconds (Fig. S1). For comparison, the data in Figure 4 of the manuscript was acquired with a delay time $\geq 87\,\mathrm{ms}$.

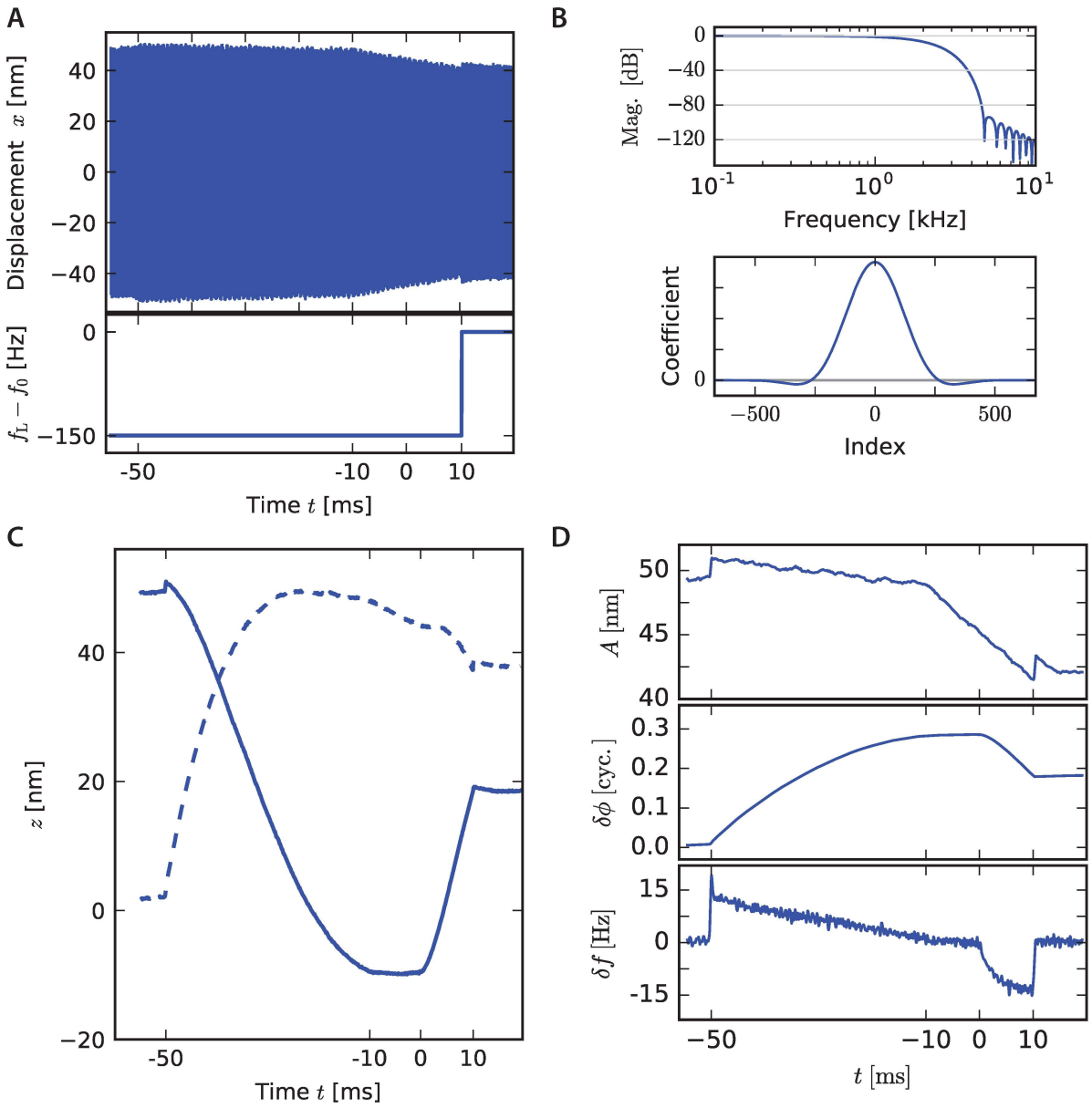

FIG. S2. **Cantilever oscillation data workup protocol**. (**A**) Cantilever displacement *versus* time data. (**B**) Lock-in filter magnitude response and coefficients. (**C**) Real (solid) and imaginary (dashed) components of the lock-in output. (**D**) Lock-in output processed into amplitude, phase, and frequency *vs*. time. At $t = -10\,\mathrm{ms}$, the cantilever drive voltage was turned off.

S2. DATA WORKUP DISCUSSION

The data workup procedure is outlined in Fig. S2. The variable-frequency lock-in amplifier used a reference frequency reflecting the expected changes to the cantilever frequency caused by

the changing tip voltage, $f_{\mathrm{L}} = f_0 - f_0 C_{\mathrm{t}}'(0) V_{\mathrm{t}}(t)^2/(4k_0)$. The resulting frequency difference is shown in Fig. S2A (bottom).

The low-pass lock-in filter H_{L} was constructed in the frequency domain, using a passband frequency f_{LP1}, below which the filter response should be 1, and a stopband frequency f_{LP2}, above which the frequency response should be 0. The frequency domain response was a Tukey window, which tapers from 1 to 0 between the passband frequency f_{LP1} and the stopband frequency f_{LP2}. The resulting time domain filter of $N = 16 f_{\mathrm{s}}/f_{\mathrm{LP1}}$ coefficients (where f_{s} is the sampling rate) was multiplied by a Blackman window to produce the final filter coefficients. The filter's 3 dB bandwidth was approximately $1.92 f_{\mathrm{LP1}}$. The filter magnitude response and time domain coefficients are shown in Fig. S2B.

The resulting complex lock-in signal z generated by the digital lock-in amplifier is

$$z[k] = H_{\mathrm{L}} * (x[k] \exp(-2\pi i f_{\mathrm{L}}[k])), \tag{S1}$$

where x is the cantilever displacement and the square brackets indicate that we work with an array of discrete data points. The points have index $k = 1, 2, 3, \ldots, N$ corresponding to times $t = k\Delta t + t_0$, where $\Delta t = 1\,\mu\mathrm{s}$ is the sampling time (inverse of the National Instruments PCI-6259's sampling rate) and the initial time t_0 is an offset used to align the start of the light pulse to $t = 0$. The asterisk ($*$) denotes a discrete convolution. From the signal z, we computed amplitude $A[k] = |z[k]|$, phase $\phi[k] = \arg z[k]$, and frequency shift $\delta f[k] = (\phi[k+1] - \phi[k-1])/(4\pi\Delta t)$, where the frequency shift is a central difference estimate of the derivative of $\phi[k]$.

The signal-to-noise ratio of the pk-EFM measurement was sensitive to the chosen phase-difference-filter time constant τ (Fig. 7D). If τ was too long, the estimated phase incorporated too much low frequency sample-induced phase noise. If τ was too short, the estimated phase was unduly influenced by high-frequency detection noise. The large low-frequency phase noise, $P_{\delta\phi} \propto f^{-3}$ (Fig. 7E), made it important to choose a relatively short τ. The time constant was chosen to be the inverse of the frequency f where

$$P_{\delta\phi}^{\mathrm{det}}(f) = P_{\delta\phi}^{\mathrm{samp}}(f) + P_{\delta\phi}^{\mathrm{therm}}(f). \tag{S2}$$

S3. WEIGHTED BEST FIT INTERCEPT FILTER

We used a weighted least squares linear filter to estimate the phase of the cantilever at the start and end of the light pulse in the pk-EFM experiment. The idea is that the cantilever phase near

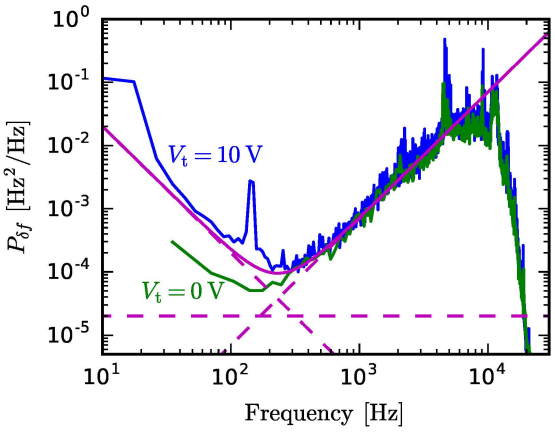

FIG. S3. **Power spectral density of cantilever frequency fluctuations**.

the start or end of the pulse is well-described by the following equations:

$$\phi(t) = \begin{cases} \phi(0) + f(0)\,t & \text{for } t \leq 0 \quad \text{(S3a)} \\ \phi(t_\mathrm{p}) + f(t_\mathrm{p})\,t & \text{for } t \geq t_\mathrm{p} \quad \text{(S3b)} \end{cases}$$

with ϕ in units of cycles. Since fast dynamics may be occurring during the pulse time, we only use data from $t \leq 0$ to determine the starting phase $\phi(0)$ and only use data from $t \geq t_\mathrm{p}$ to determine the ending phase $\phi(t_\mathrm{p})$.

Both of these equations are of the form $y = \alpha + \beta x$. Values for the best-fit intercept α and best-fit slope β were obtained by implementing a weighted least-squares fit using a time-domain filter. For equally spaced x values, α and β can be obtained using a finite-impulse-response filter [61]. For N points, we take the x-coordinates equal to $0, 1, \ldots, N-1$. For weighted least squares, we can write the resulting coefficient vector $\boldsymbol{\beta} = (\alpha\ \beta)^T$ as

$$\boldsymbol{\beta} = (\boldsymbol{x}^T W \boldsymbol{x})^{-1}\, \boldsymbol{x}^T W \boldsymbol{y}, \quad \text{(S4)}$$

where,

$$\boldsymbol{x} = \begin{pmatrix} 1 & 0 \\ 1 & 1 \\ \vdots & \vdots \\ 1 & N-1 \end{pmatrix}, \quad W = \begin{pmatrix} w_0 & & & \\ & w_1 & & \\ & & \ddots & \\ & & & w_{N-1} \end{pmatrix}, \text{ and } \quad \boldsymbol{y} = \begin{pmatrix} y_0 \\ y_1 \\ \vdots \\ y_{N-1} \end{pmatrix}. \quad \text{(S5)}$$

Then we can write the matrix multiplication as sums,

$$\boldsymbol{\beta} = \begin{pmatrix} \sum_{k=0}^{N-1} w_k & \sum_{k=0}^{N-1} k\, w_k \\ \sum_{k=0}^{N-1} k\, w_k & \sum_{k=0}^{N-1} k^2\, w_k \end{pmatrix}^{-1} \begin{pmatrix} \sum_{k=0}^{N-1} w_k y_k \\ \sum_{k=0}^{N-1} k w_k y_k \end{pmatrix} \tag{S6}$$

Call the sums in the left matrix $s_j = \sum_{k=0}^{N-1} k^j w_k$. Inverting the matrix, we have,

$$\boldsymbol{\beta} = \frac{1}{s_0 s_2 - s_1^2} \begin{pmatrix} s_2 & -s_1 \\ -s_1 & s_0 \end{pmatrix} \begin{pmatrix} \sum_{k=0}^{N-1} w_k y_k \\ \sum_{k=0}^{N-1} k\, w_k y_k \end{pmatrix} \tag{S7}$$

$$\boldsymbol{\beta} = \frac{1}{s_0 s_2 - s_1^2} \left(\sum_{k=0}^{N-1} w_k (s_2 - s_1 k) y_k,\ \sum_{k=0}^{N-1} w_k (s_0 k - s_1) y_k \right)^{\mathrm{T}}. \tag{S8}$$

The slope's filter coefficients H_β and intercept's filter coefficients H_α are just the portion of the sum excluding y_k. The filter coefficients are thus

$$H_\alpha[k] = w_k \frac{(s_2 - s_1 k)}{s_0 s_2 - s_1^2} \text{ for } k = 0, \ldots N-1 \text{ and} \tag{S9}$$

$$H_\beta[k] = w_k \frac{(s_0 k - s_1)}{s_0 s_2 - s_1^2} \text{ for } k = 0, \ldots N-1. \tag{S10}$$

For our phase-difference filter we chose a time constant τ and used exponential weights $w_k = e^{-k/(f_\mathrm{s}\tau)}$ with $N = \mathrm{round}(5 f_\mathrm{s} \tau)$. Figure 7(D and E) show the phase-difference filter coefficients and response function. A different time constant was used to fit the $\phi(t \leq 0)$ and $\phi(t \leq t_\mathrm{p})$ data sets. Each time constant was chosen empirically, to maximize the signal-to-noise ratio.

S4. REFERENCE AMPLITUDE AND PHASE SHIFT

To correctly estimate the cantilever phase shift during the pulse, we had to account for the phase shift caused by the abrupt change in tip-sample voltage at the end of the pulse. The measured phase shift $\Delta\phi$ includes both the light-induced phase shift $\Delta\phi_{h\nu}$ and the phase shift $\Delta\phi_\mathrm{ref}$ resulting from the abrupt change in the cantilever voltage at the end of the cantilever pulse: $\Delta\phi = \Delta\phi_{h\nu} + \Delta\phi_\mathrm{ref}$. First, the step change in V_t creates a frequency shift according to the standard KPFM equation (Eq. 1). Equation 1 gives the cantilever frequency ignoring any additional effects caused by abruptly changing the cantilever charge. We account for the KPFM frequency and phase shift using a variable frequency lock-in amplifier (see Supplementary Discussion S2).

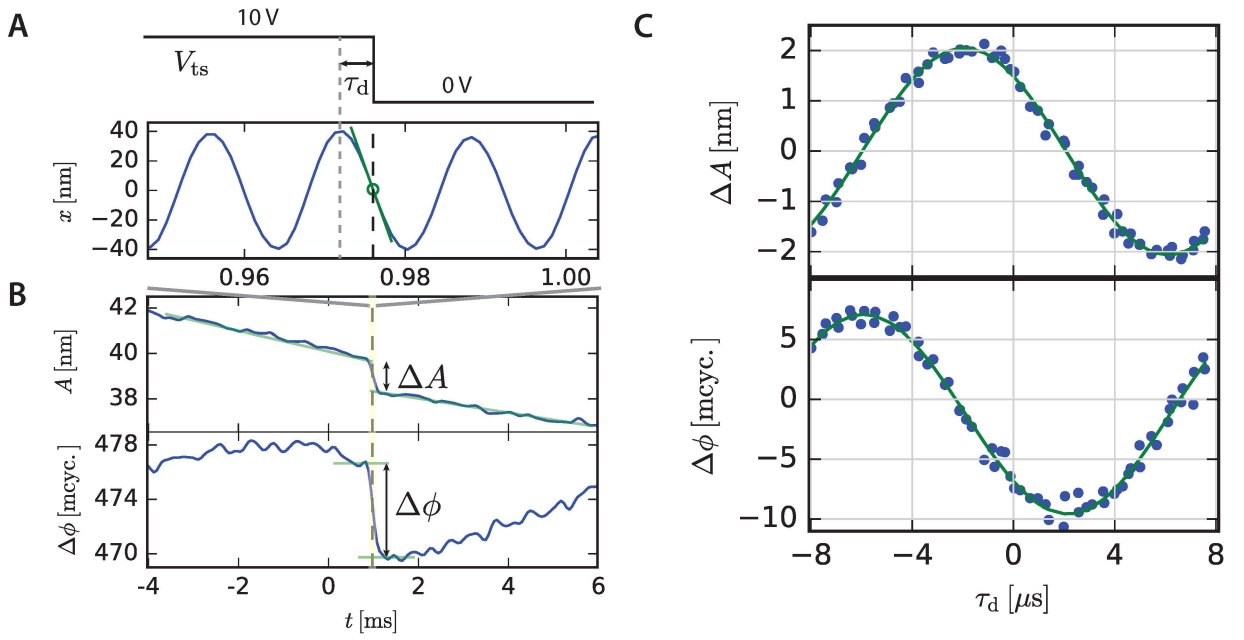

FIG. S4. **Analysis of the amplitude and phase shifts imparted by the abrupt voltage step in the pk-EFM experiment**; data from a control dataset acquired at zero light intensity at a height $h = 250\,\mathrm{nm}$ above a film of PFB:F8BT on ITO. (**A**) The end of the tip voltage pulse occurs at time τ_d relative to the cantilever oscillation cycle, with $\tau_\mathrm{d} = 0$ defined as the time at which the cantilever reaches its maximum extension. (**B**) The resulting amplitude and phase shifts caused by abruptly turning off the tip voltage. (**C**) The amplitude and phase shifts for each pulse are plotted *versus* the delay time t_d. The amplitude and phase shifts imparted by the abrupt change at the end of the voltage pulse depend on τ_d, as described by Eqs. 21 and 22. Amplitude best-fit parameters: $A_\mathrm{max} = 2.06 \pm 0.02\,\mathrm{nm}$, $\theta = -136.6 \pm 0.7\,\mathrm{deg.}$, and $\Delta A_0 = 0.01 \pm 0.02\,\mathrm{nm}$. Phase best-fit parameters: $\phi_\mathrm{max} = 8.3 \pm 0.1\,\mathrm{mcyc}$, $\theta = -137.9 \pm 0.9\,\mathrm{deg.}$, and $\Delta\phi_0 = -1.3 \pm 0.1\,\mathrm{mcyc}$.

To account for the phase and amplitude shifts caused by the step change to the tip-sample voltage, we use Eqs. 21 and 22 to model the additional impulsive phase shift and amplitude shift delivered by the end of the pulse. As shown in Fig. S4, we fit the control data to the equation

$$\Delta A_\mathrm{mod}(t_\mathrm{d}) = -A_\mathrm{max}\cos(2\pi f_\mathrm{c} t_\mathrm{d} + \theta) + \Delta A_0 \tag{S11a}$$

$$\Delta\phi_\mathrm{mod}(t_\mathrm{d}) = \quad \phi_\mathrm{max}\sin(2\pi f_\mathrm{c} t_\mathrm{d} + \theta) + \Delta\phi_0, \tag{S11b}$$

with fitting parameters A_max, the maximum amplitude; ϕ_max, the maximum phase shift; θ, a phase offset accounting for the detector delay; ΔA_0, an amplitude offset; and ϕ_0, a phase-shift offset. The magnitudes of the amplitude and phase corrections are self-consistent. From Eqs. 21 and 22, we

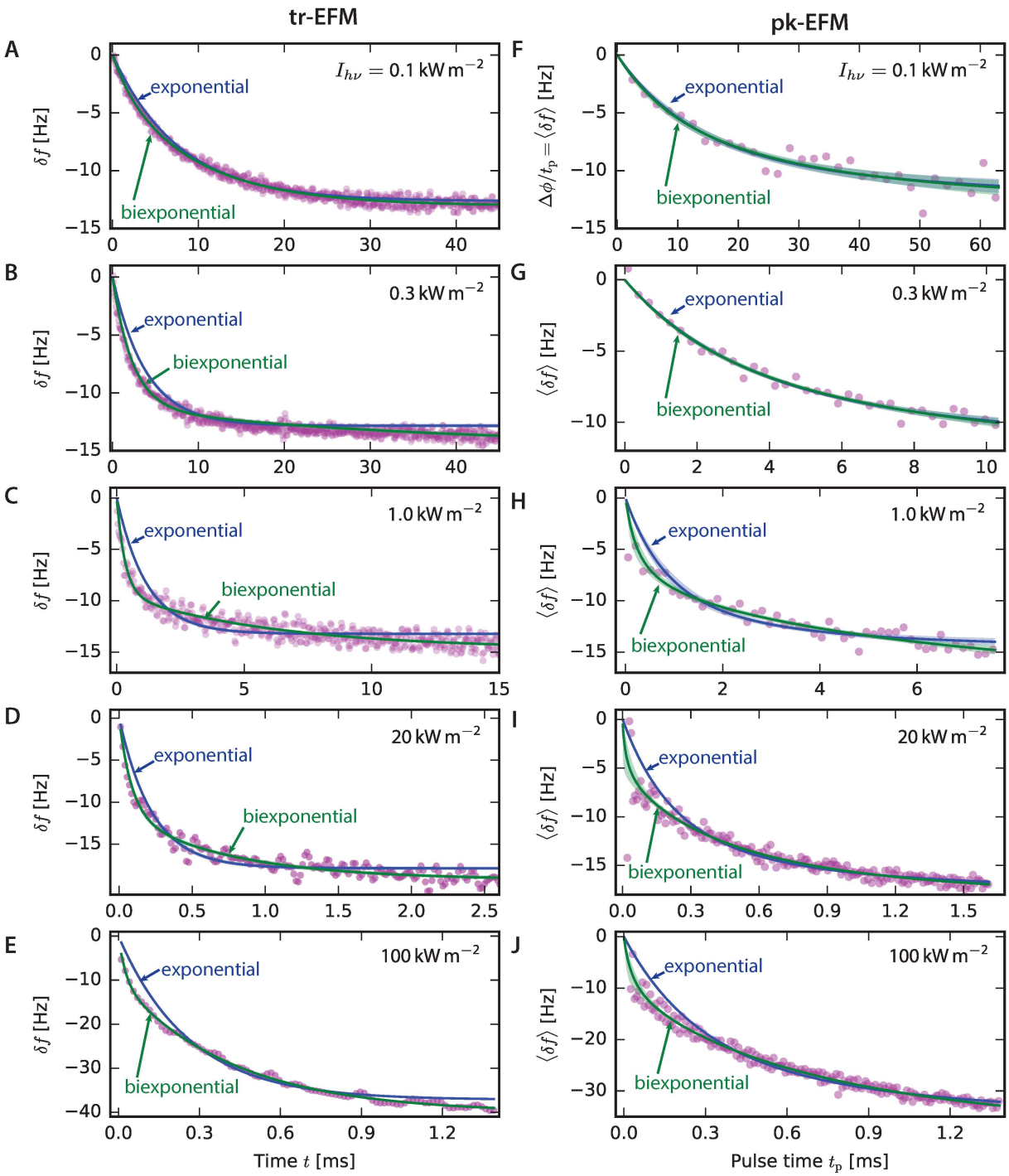

FIG. S5. **Comparison of single and biexponential fits to tr-EFM and pk-EFM data.** (**A**–**E**) tr-EFM data (purple points) fitted to single exponential (blue curve) and biexponential (green curve) frequency shift models. (**F**–**J**) pk-EFM data (purple points) fitted to single exponential (blue curve) and biexponential (green curve) frequency shift models. The purple data points are the average of two (**F** – **H**) or four (**I**–**J**) adjacent pulse times. The blue and green regions show the 5th to 95th percentile of the single and biexponential curve fits respectively, determined from $N = 6000$ MCMC samples. Experimental parameters: PFB:F8BT on ITO, $h = 250\,\mathrm{nm}$, and $V_\mathrm{t} = 10\,\mathrm{V}$.

have

$$\Delta\phi_{\max} = \Delta A_{\max}/A_0 = 2.06\,\mathrm{nm}/40\,\mathrm{nm} = 8.2\,\mathrm{mcyc}, \tag{S12}$$

which is within the error bar of the measured value of $\Delta\phi_{\max} = 8.3 \pm 0.1\,\mathrm{mcyc}$. The phase offsets θ from the amplitude and phase fits are also self-consistent. As the equations are defined, the two phases ϕ should be strictly equal. The calculated best fit values for ϕ differ by 1.3 ± 1.1 deg.

S5. BIEXPONENTIAL CURVE FITS

Figure S5 compares single and biexponential curve fits to the data of Figure 4. Both models adequately fit the $0.1\,\mathrm{kW\,m^{-2}}$ tr-EFM data (A). At all higher light intensities (B–E), the single exponential model does not fit the tr-EFM data as well. In each case, the single exponential model does not have enough degrees of freedom to capture both the initial rapid change in cantilever frequency shift and the slow, extended movement towards equilibrium.

For the pk-EFM data, we plot the average cantilever frequency shift during the pulse $\langle \delta f \rangle = \Delta\phi(t_\mathrm{p})/t_\mathrm{p}$ to highlight the difference between the two models at short pulse times t_p. Both models adequately fit the $0.1\,\mathrm{kW\,m^{-2}}$ pk-EFM data (Fig. S5F). The $0.3\,\mathrm{kW\,m^{-2}}$ pk-EFM data (G) is collected over a much shorter range of pulse times (0 to $10\,\mathrm{ms}$) than the $0.3\,\mathrm{kW\,m^{-2}}$ tr-EFM data (B, $45\,\mathrm{ms}$), so both models are still able to adequately capture the dynamics over this shorter period of time. For the higher intensity pk-EFM data (H–J), the single exponential model misses the short time dynamics as it did for the tr-EFM data. Overall, the pk-EFM data is consistent with the tr-EFM data, and in both cases a single exponential model fits the data poorly.

S6. ALTERNATIVE EXPLANATIONS OF PHOTOCAPACITANCE DYNAMICS

At the highest light intensities ($I_{h\nu} = 20\,\mathrm{kW\,m^{-2}}$ and $100\,\mathrm{kW\,m^{-2}}$), the timescale of the fast component of the sample dynamics starts to approach the cantilever's characteristic timescale $\omega_\mathrm{c}^{-1} = 2.6\,\mu\mathrm{s}$ (Fig. 4D). In this case, the effect of the forcing term $\mathbf{b}(t) \propto C_\mathrm{t}'(t)$ must be considered. The situation is similar to the one considered in Equation 23, but the pulse time t_p used in the tr-EFM and pk-EFM experiments of Figure 4 is usually longer than a cantilever period. In this case, the approximate additional cantilever position shift induced by the light pulse is

$$\Delta x_{h\nu}^F(t>0) = \underbrace{\delta x_{h\nu}\left(1 - \frac{\omega_\mathrm{c}^2\tau_\mathrm{x}^2}{1+\omega_\mathrm{c}^2\tau_\mathrm{x}^2}e^{-t/\tau_\mathrm{x}}\right)}_{\text{shift in cantilever DC displacement}} - \underbrace{\frac{\delta x_{h\nu}}{1+\omega_\mathrm{c}^2\tau_\mathrm{x}^2}(\cos\omega_\mathrm{c}t + \omega_\mathrm{c}\tau_\mathrm{x}\sin\omega_\mathrm{c}t)}_{\text{oscillation at the cantilever frequency}}. \tag{S13}$$

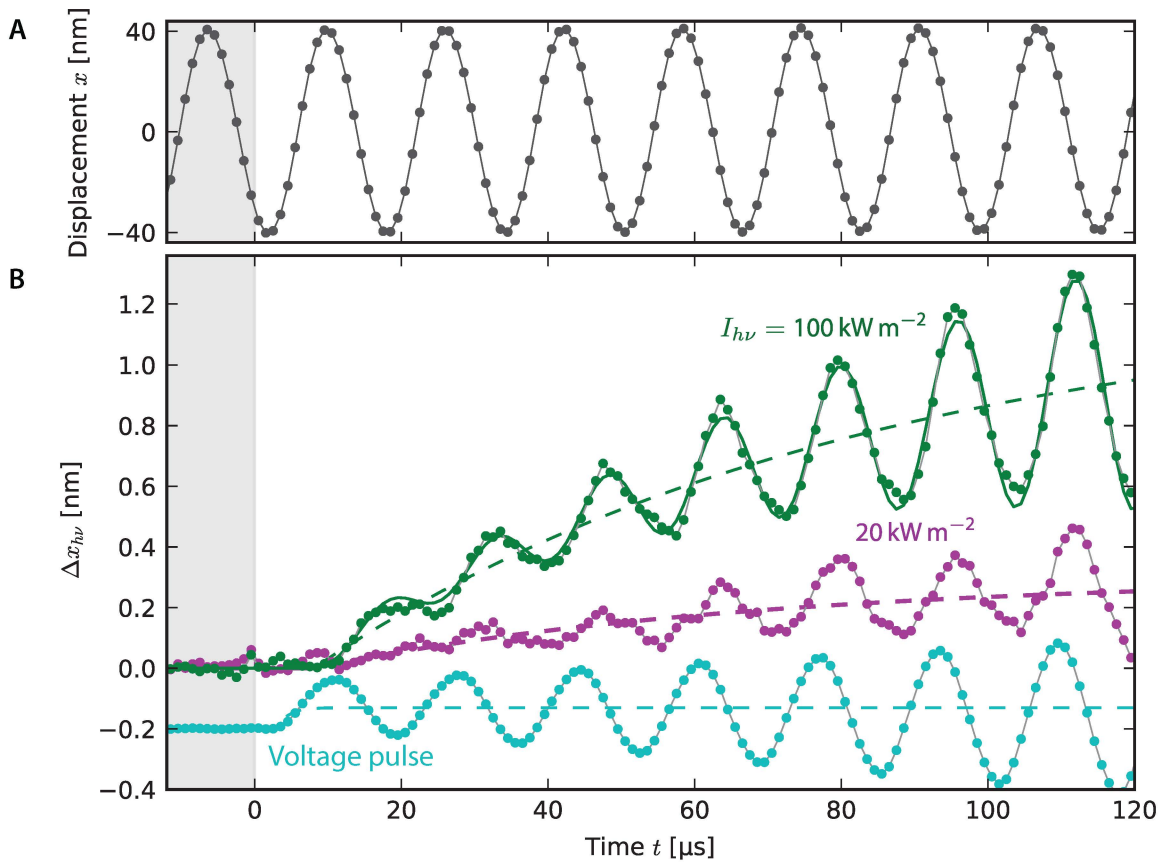

FIG. S6. **Light-induced changes in cantilever displacement**. (**A**) Signal-averaged displacement *versus* time data from the $I_{h\nu} = 100\,\mathrm{kW\,m^{-2}}$ dataset. Best-fit parameters for the model of Equation S14: $X_0 = -22.551 \pm 0.003\,\mathrm{nm}$, $Y_0 = 34.687 \pm 0.003\,\mathrm{nm}$, $f_1 = 61\,840.51 \pm 0.01\,\mathrm{Hz}$, and $Q = 22\,000 \pm 200$. **(B)** Light-induced changes in displacement for the $I_{h\nu} = 100\,\mathrm{kW\,m^{-2}}$ and $20\,\mathrm{kW\,m^{-2}}$ intensity tr-EFM experiments. The voltage-induced position shift from Figure 5K is plotted for comparison (scaled and offset: we plot $0.05\Delta x_V(t) - 0.2\,\mathrm{nm}$). The dashed lines show the evolution of the DC cantilever displacement (first term of Eq. S13). The green curve shows the best-fit parameters for the model of Equation S16: $\tau_\mathrm{x} = 69 \pm 2\,\mu\mathrm{s}$, $t_0 = 6.6 \pm 0.4\,\mu\mathrm{s}$, $\delta x_{h\nu} = 1.16 \pm 0.01\,\mathrm{nm}$, $X_1 = -4.3 \pm 0.1\,\mathrm{nm}$, $Y_1 = 0.3 \pm 0.7\,\mathrm{nm}$, and $\tau_{\delta f} = 18 \pm 4\,\mu\mathrm{s}$.

The first term is just the expected DC cantilever deflection resulting from a change in tip-sample force F. This term is filtered out by the lock-in amplifier filter when we measure cantilever amplitude or phase. The second term shows that the force induces an oscillation at the cantilever frequency with amplitude $A_\mathrm{x} = \delta x_{h\nu}/\sqrt{1+\omega_\mathrm{c}^2\tau_\mathrm{x}^2}$. For the cantilever frequency, we use $\omega_\mathrm{c} = \omega_0 + \delta\omega(t=0)$. We use τ_x to allow for the possibility that the time constant associated with the forcing term may be different than the time constant(s) associated with the force gradient term ($\Delta\phi(t)$ and $\delta f(t) \propto C_\mathrm{t}''$).

To assess the size of this short-time effect, we examine the $100\,\mathrm{kW\,m^{-2}}$ signal-averaged tr-EFM data set in the time domain (Figure S6A). To see the effect of the light pulse on the cantilever motion at very short times, we fit the cantilever data *before* the light was turned on, when the cantilever was oscillating at a fixed frequency with a slowly decaying amplitude to a damped sinusoid (x_{DHO}). The residuals have a standard deviation of $21\,\mathrm{pm}$. If the light had no effect on the tip-sample force, we would expect the cantilever to continue oscillating at its resonance frequency with a slowly decaying amplitude as described by the fit from $t < 0$. To isolate the effect of the light, Figure S6B plots the difference between the measured cantilever displacement $x(t)$ and the expected cantilever motion $x_{\mathrm{DHO}}(t)$. This light-induced displacement $\Delta x_{h\nu}(t) = x(t) - x_{\mathrm{DHO}}(t)$ reflects changes to both the force $\mathbf{b}(t)$ on the cantilever and the cantilever's resonance frequency (Equation 1). The effect of the forcing term $\mathbf{b}(t)$ is purely additive (Equation 12), so we can estimate the rise time of the C' term and the change in displacement $\delta x_{h\nu}$ directly from Figure S6B. For the $100\,\mathrm{kW\,m^{-2}}$ dataset, we find a $\delta x_{h\nu} = 1.16 \pm 0.02\,\mathrm{nm}$ position shift induced by the light with a time constant $\tau_{\mathrm{x}} = 69 \pm 4\,\mu\mathrm{s}$ (2σ uncertainties). The corresponding induced oscillation amplitude is $A_{\mathrm{x}} = 43\,\mathrm{pm}$. The induced oscillation is almost exactly 90 degrees out of phase with the cantilever motion, so the total phase shift caused by the neglected $\mathbf{b}(t)$ dynamics is $\Delta\phi_{\mathrm{x}} = A_{\mathrm{x}}/A_0 = 0.17 \pm 0.01\,\mathrm{mcyc}$, where $A_0 = 41.4\,\mathrm{nm}$ is the amplitude of the cantilever oscillation at $t = 0$ (Figure S6A, see Equation 22). This phase shift is insignificant compared to the phase shift induced by the cantilever frequency shift (Fig. 4A).

In summary, the model derived from the pk-EFM theory fits the cantilever's short time dynamics well (data analysis described below in section S7). At $100\,\mathrm{kW\,m^{-2}}$, the surface potential measured at long times shifted by $\Delta\Phi_{h\nu} = +440\,\mathrm{mV}$. On its own, this would correspond to a cantilever frequency shift of $\Delta f = 15\,\mathrm{Hz}$; in contrast, the total measured frequency shift, including contributions from both shifts in tip-sample capacitance and surface potential was $-41\,\mathrm{Hz}$. The experiments here do not preclude a shift in surface potential contributing to the measured position and frequency shift. However, the data of Figure S6B does make it unlikely that the fast dynamics are wholly explained by surface potential shifts. Since there is no evidence of a positive frequency shift Δf in Figure S5 or a negative position shift $\Delta x_{h\nu}(t)$ in S6, the transient surface potential shift would either have to be *negative* (compared to positive at long times), or always masked by a larger negative frequency shift induced by the change in photocapacitance.

S7. TIME DOMAIN CANTILEVER OSCILLATION FITS

See section S6 for the motivation of this model. We fit the signal-averaged position data from $t = -1.5\,\mathrm{ms}$ to $t = 0$ to a damped, variable frequency sinusoid:

$$x_{\mathrm{DHO}}(t; X_0, Y_0, f_1, Q) = e^{-\pi f_1 t/Q}\left(X_0\cos(2\pi f_1 t) + Y_0\sin(2\pi f_2 t)\right) \tag{S14}$$

The fit parameters are the cantilever phase factors X_0, Y_0, frequency f_1, and quality factor Q. While this is a good model of the cantilever motion, it neglects the non-linearity of our interferometer position detector. To account for this non-linearity (see supplementary text S8, Fig. S7), we performed a linear, least-squares fit of the residuals $r_{\mathrm{DHO}}(t) = x(t) - x_{\mathrm{DHO}}(t)$ to the equation

$$f_{\mathrm{harm.}}(t, f_1; X_n, Y_n) = \sum_{n=2}^{5}(X_n\cos(2\pi n f_1 t) + Y_n\sin(2\pi n f_1 t)). \tag{S15}$$

The fit parameters were the weights $X_2, Y_2 \ldots X_5, Y_5$. This fit removes the components of the residuals at the second through fifth harmonics of the cantilever frequency which are phase-locked to the cantilever oscillation (see Fig. S7). The frequency f_1 was fixed equal to the value determined from the fit of Equation S14. The resulting light-induced displacement $\Delta x_{h\nu}(t) = x(t) - x_{\mathrm{DHO}}(t) - f_{\mathrm{harm.}}(t)$ are plotted in Figure S6B.

The light-induced displacement was fit to the equation

$$f(t' = t - t_0, \omega_{\mathrm{c}}; \tau_{\mathrm{x}}, \delta x_{h\nu}, t_0, X_1, Y_1, \tau_{\delta f}) = \Delta x^F_{h\nu}(t') + \left[X_1\cos(\omega_{\mathrm{c}} t) + Y_1\sin(\omega_{\mathrm{c}} t)\right]\Delta\phi(t', \tau_{\delta f}) \tag{S16}$$

where the fit parameters were the rise time τ_{x} of the light-induced change in C', the light-induced change in DC displacement $\delta x_{h\nu}$, the time at which the light pulse began t_0, phase factors X_1, Y_1, and the timescale of changes to the cantilever frequency $\tau_{\delta f}$ (the usual τ found from the data of Figure 4). The phase shift $\Delta\phi$ was the single exponential rise time phase shift from Equation 19, with $t_{\mathrm{p}} = t - t_0$. The magnitude of the phase shift is determined by the size of X_1, Y_1 compared to X_0, Y_0 from the fit of Equation S14. The cantilever frequency ω_{c} was fixed equal to $2\pi f_1$, with f_1 determined from Equation S14.

The time-domain fits in Figure 5J–L are carried out in the same way. In this case, however, the contribution of the photodetector high pass filter response time $\tau_{\mathrm{HP}} = \omega_{\mathrm{HP}}^{-1} = 530\,\mu\mathrm{s}$ is significant. The high pass filter's step response to an input of magnitude $\delta x_{h\nu}$ is approximated by $\delta x_{h\nu}\exp(-t'/\tau_{\mathrm{HP}})$, so the slow decay of the DC component of Δx^F is approximated by subtracting $\delta x_{h\nu} t'/530\,\mu\mathrm{s}$. This is a good approximation when $\tau_{\mathrm{c}} \ll \tau_{\mathrm{HP}}$ and $t' > 3\tau$.

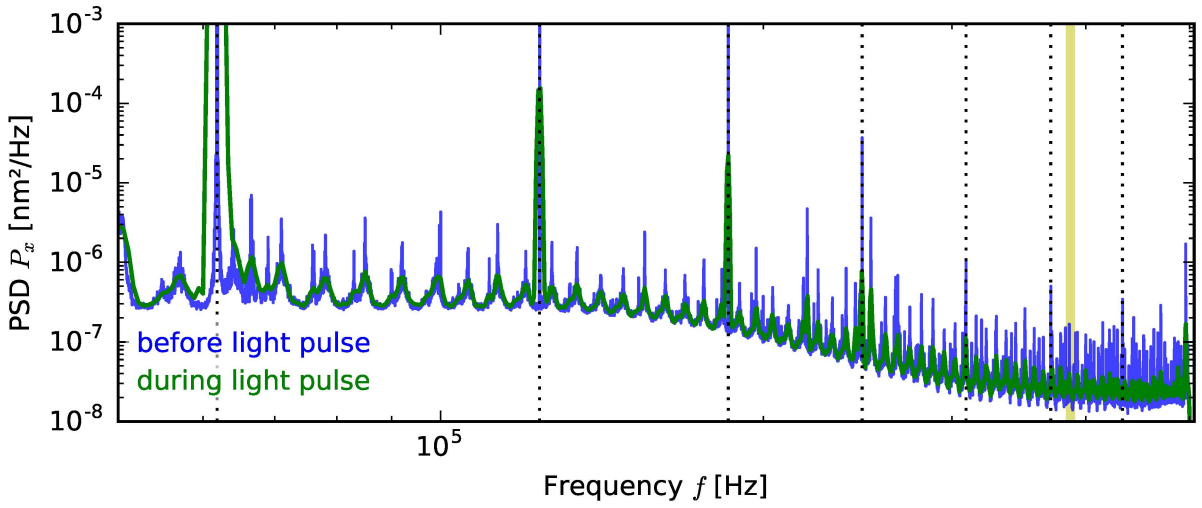

FIG. S7. **Cantilever position power spectral density during tr-EFM.** Power spectra calculated from signal-averaged $100\,\mathrm{kW\,m^{-2}}$ tr-EFM position *vs.* time data ($N = 784$, see data in Fig. 4 and S5E). The *before light pulse* curve (blue) uses data from $t = -50\,\mathrm{ms}$ to 0. The *during light pulse* curve (green) uses data from $t = 0$ to $1.75\,\mathrm{ms}$. The dotted lines show the harmonics of the cantilever's first resonance frequency ($f_0 = 62\,000\,\mathrm{Hz}$). The shaded yellow region shows where the cantilever's second resonance frequency would be ($f_{res.}^{2\mathrm{nd}} = 6.27 f_0$, from Euler-Bernoulli beam theory). Both spectral densities were calculated using a Blackman window. Experimental parameters: PFB:F8BT on ITO, $h = 250\,\mathrm{nm}$, and $V_\mathrm{t} = 10\,\mathrm{V}$.

S8. HIGHER CANTILEVER EIGENMODES

Figure S7 shows that even at the highest light intensity, we do not excite higher cantilever resonances. The peaks at harmonics of the cantilever's first resonance frequency appear because we detect motion with an interferometer, so we detect $\delta x_\mathrm{meas}(t) \propto V_\mathrm{photodetector} \propto \sin\left(4\pi[x_0 + \delta x(t)]/\lambda\right)$, where x_0 is the distance between the fiber and cantilever with no drive or tip-sample voltage, δx is the cantilever's displacement, and $\lambda = 1488\,\mathrm{nm}$ is the interferometer wavelength. The sine term gives rise to odd harmonics of the cantilever frequency in the position spectrum ($\sin x = x - x^3/3! + x^5/5! + \ldots$). Since $4\pi x_0/\lambda$ is not exactly a multiple of π, there is also a small cosine term which gives rise to even harmonics of the cantilever frequency. The roll-off of the measured displacement noise is caused by our photodetector's $200\,\mathrm{kHz}$ bandwidth.

The voltage step at the end of the light pulse does not excite the cantilever's higher resonance modes either, as shown in Figure S8. We also see no evidence that the cantilever's higher resonance modes are appreciably excited by the 50 to $800\,\mathrm{ns}$ voltage pulses applied during the experiments

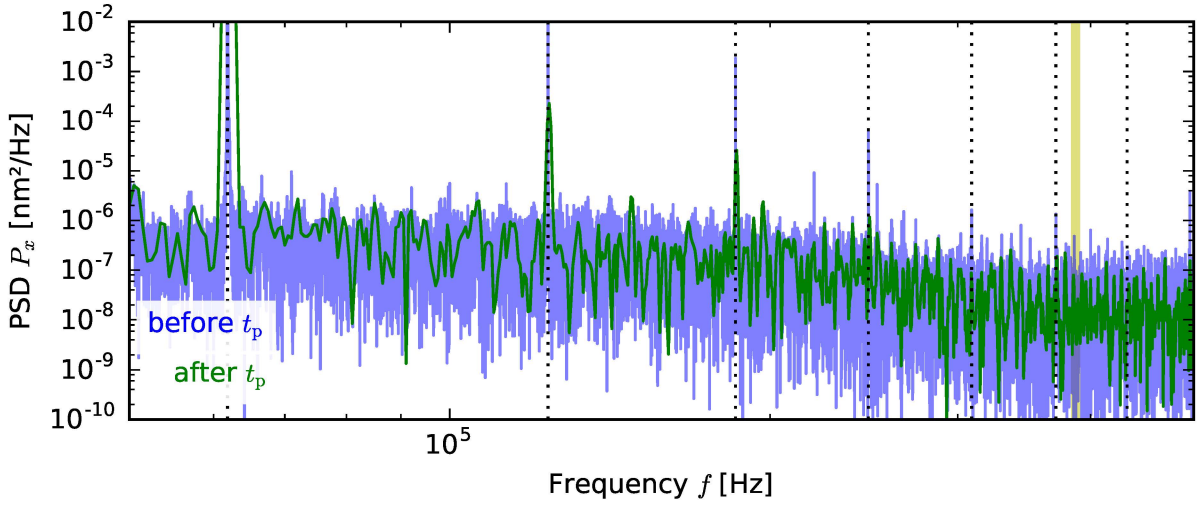

FIG. S8. **Cantilever position power spectral density during pk-EFM.** Power spectral density calculated from the $20\,\mathrm{kW\,m^{-2}}$ pk-EFM position *vs.* time data (see data in Fig. 4 and S5I). The power spectral density was calculated from the shortest pulse time dataset ($t_\mathrm{p} = 0.8\,\mu\mathrm{s}$). The *before* t_p curve (blue) uses data from $t = -50\,\mathrm{ms}$ to $t_\mathrm{p} = 0.8\,\mu\mathrm{s}$. The *after* t_p curve (green) uses data from $t = t_\mathrm{p} = 0.8\,\mu\mathrm{s}$ to $t_\mathrm{p} + 2\,\mathrm{ms} = 2.0008\,\mathrm{ms}$, when the cantilever could conceivably be excited at a higher resonance mode. The dotted lines show the harmonics of the cantilever's first resonance frequency $f_0 = 62\,000\,\mathrm{Hz}$. The shaded yellow region shows where the cantilever's second resonance frequency would be ($f_{res.}^{2\mathrm{nd}} = 6.27 f_0$, from Euler-Bernoulli beam theory). Both spectral densities were calculated using a Blackman window. Experimental parameters: PFB:F8BT on ITO, $h = 250\,\mathrm{nm}$, and $V_\mathrm{t} = 10\,\mathrm{V}$.

of Figure 6A–F. Even if higher resonance modes were excited a small amount, the digital lock-in amplifier filters used in the data workup strongly reject frequencies more than a few kilohertz from the cantilever's first resonance frequency. Figure S2 shows that $10\,\mathrm{kHz}$ away from the cantilever resonance frequency, the lock-in amplifier filter transfer function's magnitude response is $-120\,\mathrm{dB} = 10^{-6}$.

S9. PHOTOTHERMAL EFFECTS

We rule out cantilever heating because with the light on, we find no significant change in the cantilever's resonance frequency f_0.

Next we consider sample heating. The sample is a thin PFB:F8BT layer ($\sim 100\,\mathrm{nm}$) on a thin indium tin oxide (ITO) layer ($\sim 700\,\mathrm{nm}$) on a thick glass substrate ($1.1\,\mathrm{mm}$). An upper limit for the temperature change ΔT is obtained by neglecting the relatively high thermal conductivity ITO

layer and assuming that all of the incident light is absorbed in the PFB:F8BT layer. We assume the PFB:F8BT layer can be approximated as constant temperature, and solve for the steady-state temperature increase by considering the diffusion of heat into the glass substrate, which we treat as semi-infinite. Cahill gives the steady-state temperature increase in Equation 11 of Ref. 62:

$$\Delta T_0 = \frac{P_{h\nu}}{2\sqrt{\pi} w_0 \Lambda}. \tag{S17}$$

At the highest light intensity ($I_{h\nu} = 100\,\mathrm{kW\,m^{-2}}$), the laser power $P_{h\nu} = 3\,\mathrm{mW}$. At the sample surface, the beam shape is elliptical with $330\,\mu\mathrm{m}$ and $120\,\mu\mathrm{m}$ major and minor axes (diameters). We approximate the beam radius w_0 by considering a circular beam of equivalent area: $w_0 = \sqrt{120\,\mu\mathrm{m} \times 330\,\mu\mathrm{m}/4} = 100\,\mu\mathrm{m}$. We take the thermal conductivity Λ of the glass substrate to be $1.0\,\mathrm{W\,m^{-1}\,K^{-1}}$. In this case, the DC temperature rise $\Delta T_0 = 8.5\,\mathrm{K}$. This analysis is broadly consistent with the calculation performed by Luria and coworkers in Supplementary Note 5 of Ref. 63.

Even this temperature change is small, given the large tip-sample separation ($h = 250\,\mathrm{nm}$). The temperature change for our $1.5\,\mathrm{ms}$ and shorter light pulses is even smaller. The frequency ω_{heat} at which the system reaches the steady-steady temperature calculated above is

$$\omega_{\mathrm{heat}} = \frac{\Lambda}{\pi w_0^2 C_{\mathrm{P}} \rho}, \tag{S18}$$

where $C_{\mathrm{P}} = 840\,\mathrm{J\,kg^{-1}\,K}$ and $\rho = 840\,\mathrm{kg\,m^{-3}}$ are the specific heat capacity and density of the glass substrate respectively. The corresponding timescale is $\omega_{\mathrm{heat}}^{-1} = 20\,\mathrm{ms}$, significantly longer than the pulse time $t_{\mathrm{p}} \sim 1\,\mathrm{ms}$. The temperature change in this limit is given by Cahill's Eq. 13:

$$\Delta T = \frac{P_{h\nu}}{\pi w_0^2 \sqrt{\omega \Lambda C_{\mathrm{P}} \rho}}. \tag{S19}$$

Evaluating this equation at $\omega = (1.5\,\mathrm{ms})^{-1}$, we find a temperature change of only $2.1\,\mathrm{K}$.

S10. NUMERICAL SIMULATIONS

The numerical simulations shown in Fig. 6D were performed for the following system of ordinary differential equations:

$$\dot{x} = v \tag{S20}$$

$$\dot{v} = -\omega_0^2 x - \frac{\omega_0}{Q} v + \frac{C_{\mathrm{t}}'}{2mC_{\mathrm{t}}^2}(1+\alpha_{h\nu})q_{\mathrm{t}}^2 + \frac{C_{\mathrm{t}}''}{2mC_{\mathrm{t}}^2}(1+\alpha_{h\nu})xq_{\mathrm{t}}^2 + \frac{F_{\mathrm{n}}(t)}{m} \tag{S21}$$

$$\dot{q}_{\mathrm{t}} = \frac{-q_{\mathrm{t}}}{R_{\mathrm{t}}}C^{-1}(x) + \frac{1}{R_{\mathrm{t}}C_1}q_1 \tag{S22}$$

$$\dot{q}_1 = \frac{q_{\mathrm{t}}}{R_{\mathrm{t}}}C^{-1}(x) - \left(\frac{1}{C_1R_1} + \frac{1}{R_{\mathrm{t}}C_1}\right)q_1 - \frac{\phi}{R_1} + \frac{V_{\mathrm{t}}(t)}{R_1} \tag{S23}$$

$$\dot{\alpha}_{h\nu} = -\frac{1}{\tau_{\mathrm{s}}}\alpha_{h\nu} + \frac{I_{h\nu}(t)}{\tau_{\mathrm{s}}} \tag{S24}$$

$$\dot{\phi} = \phi_{\mathrm{n}}(t). \tag{S25}$$

The state vector variables were cantilever displacement x, cantilever velocity v, cantilever tip charge q_{t}, cabling charge q_1, fractional change in photocapacitance $\alpha_{h\nu}$, and surface potential ϕ. The cantilever parameters were mass $m = 46\,\mathrm{ng}$, spring constant $k_0 = 7\,\mathrm{N/m}$, resonance frequency $\omega_0 = \sqrt{k_0/m} = 2\pi \times 62\,\mathrm{kHz}$ and quality factor $Q = 2.7 \times 10^4$. In writing these equations the tip-sample capacitance $C(x)$ was linearized as follows:

$$C(x) = C_{\mathrm{t}} + C_{\mathrm{t}}'(1+\alpha_{h\nu})x + \frac{1}{2}C_{\mathrm{t}}''(1+\alpha_{h\nu})x^2 \tag{S26}$$

$$C^{-1}(x) = C_{\mathrm{t}}^{-1} + \frac{C_{\mathrm{t}}'(1+\alpha_{h\nu})x}{C_{\mathrm{t}}^2} + \frac{C_{\mathrm{t}}''(1+\alpha_{h\nu})x^2}{2C_{\mathrm{t}}^2}. \tag{S27}$$

The linearized tip-sample capacitance and its derivatives were $C_{\mathrm{t}} = 0.01\,\mathrm{pF}$, $C_{\mathrm{t}}' = 1.14 \times 10^{-4}$ $\mathrm{pF\,\mu m^{-1}}$, and $C_{\mathrm{t}}'' = 6.72 \times 10^{-4}\,\mathrm{pF\,\mu m^{-2}}$. The other circuit elements were the tip resistance $R_{\mathrm{t}} = 100\,\Omega$, cabling resistance $R_1 = 3\,\Omega$, cabling capacitance $C_1 = 10\,\mathrm{pF}$, and the input tip voltage $V_{\mathrm{t}}(t)$ ($10\,\mathrm{V}$ during the pulse, as in Fig. 2). The light "intensity" was $I_{h\nu} = 0.4$ for $t > 0$, corresponding to a total change in capacitance of 40 percent for $t \gg \tau_{\mathrm{s}}$. Simulations were performed for photocapacitance rise times $\tau_{\mathrm{s}} = 2\,\mathrm{ns}, 10\,\mathrm{ns}$ and $50\,\mathrm{ns}$.

The inputs $F_{\mathrm{n}}(t)$ and $\phi_{\mathrm{n}}(t)$ account for thermal and surface-potential noise. Both noise terms are approximated using a piecewise function with Gaussian, randomly distributed values. The force noise function $F_{\mathrm{n}}(t)$ takes a new random value every $\Delta t_{\mathrm{F}} = 16\,\mathrm{ps}$. The surface potential noise function $\phi_{\mathrm{n}}(t)$ takes a new random value every $\Delta t_\phi = 10\,\mu\mathrm{s}$. The variance of the Gaussian

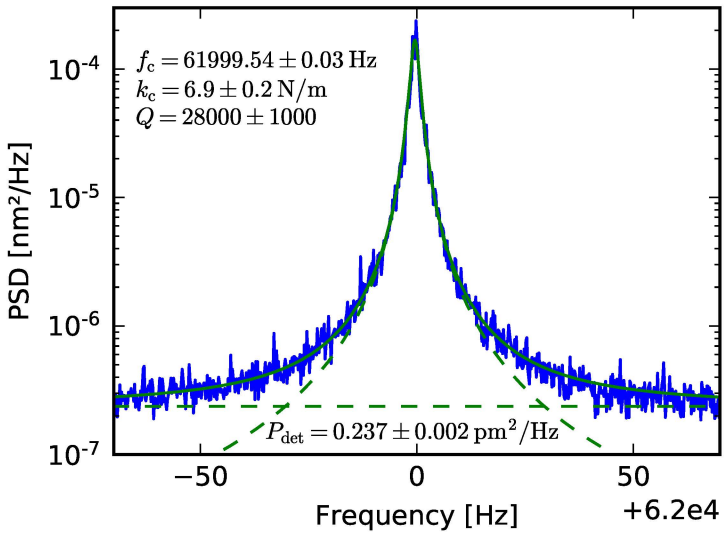

FIG. S9. **Power spectral density of cantilever thermomechanical position fluctuations**. The displayed data was calculated by signal-averaging 32 power spectra each calculated from 5 s of interferometer displacement data (sampling rate 1 MHz).

random numbers used to mimic the force noise was

$$\sigma_{F_n}^2 = \frac{k_0 k_B T}{\pi Q f_0 \Delta t_F}$$

with $T = 293\,\mathrm{K}$ the temperature and $f_0 = 62\,\mathrm{kHz}$ the cantilever frequency. The standard deviation of the potential fluctuations was taken to be $\sigma_\phi = 10\,\mu\mathrm{V}\,\mu\mathrm{s}^{-1}$. The experimental power spectral density of cantilever frequency fluctuations had a $1/f$ character at low offset frequency f. Such $1/f$ noise is difficult to implement in a numerical simulation. The slowly varying potential produced low-frequency f_c noise having a $P_{\delta f_c} \propto 1/f^2$ power spectrum and a variance approximately equal to that of the low-frequency f_c fluctuations seen experimentally (Fig. S3).

Simulations were performed with the Julia language package ODE, using a variable time step, stiff solver to handle the wide range of timescales present in the system.

S11. CANTILEVER CHARACTERIZATION

Figure S9 shows the power spectral density of cantilever position fluctuations. The extracted parameters are the cantilever frequency $f_0 = 61999.54 \pm 0.03\,\mathrm{Hz}$, cantilever spring constant $k_0 = 6.9 \pm 0.2\,\mathrm{N\,m^{-1}}$, quality factor $Q = 28000 \pm 1000$, and detector noise floor $P_{\mathrm{det}} = 0.237 \pm 0.002\,\mathrm{pm^2\,Hz^{-1}}$.

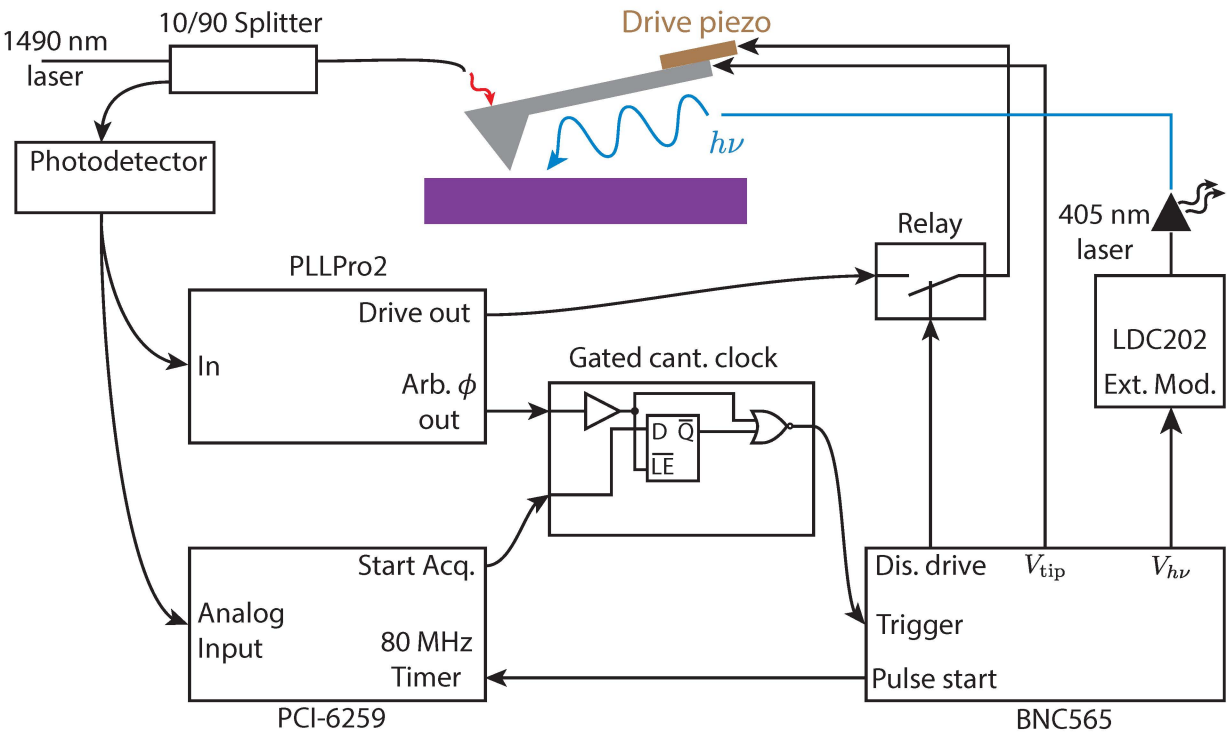

FIG. S10. **Block diagram showing the experimental setup and timing circuitry**.

S12. EXPERIMENTAL TIMING

The start of the light pulse was triggered at a consistent point in the cantilever oscillation, and step changes to the cantilever tip voltage and drive signal were also precisely timed [27]. The circuit and instruments used to control this timing are shown in Fig. S10. The photodetector output (upper left) was the cantilever displacement signal. The PLLPro2 generated the cantilever drive voltage and also output a $1\,\mathrm{V}$, phase-shifted sine wave copy of the cantilever oscillation, generated by an internal lock-in amplifier coupled to the phase-locked loop (Arb. ϕ out on diagram). A homebuilt gated cantilever clock circuit converted this $1\,\mathrm{V}$ phase-shifted sine wave to a square wave, which was used as a clock for timing tip voltage and light pulses. A $5\,\mathrm{V}$ digital signal output by the National Instruments PCI-6259 gates the clock, controlling the start of the experiment.

The BNC565 was used to trigger all signals relative to the cantilever clock. The $50\,\mathrm{ms}$ delay between the setting of the cantilever tip voltage to $10\,\mathrm{V}$ and the start of the light pulse was coded as an $N = 3100\,\mathrm{cyc}$ delay in the BNC565. The pulse lengths, times, and adjustable voltage output levels (for the tip-sample voltage, visible light laser external modulation input) for the BNC565 were programmed using GPIB in LabView.

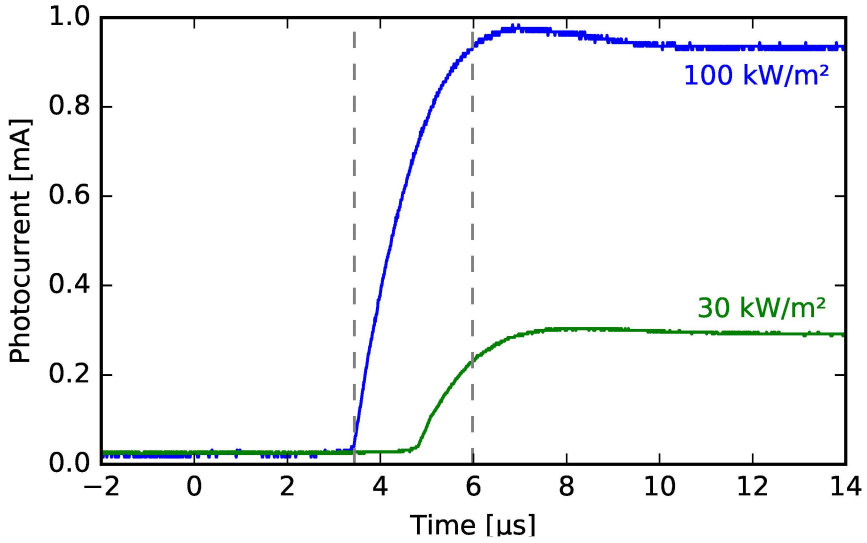

FIG. S11. **Photocurrent delay and rise time**. At $t = 0$, the voltage pulse which controls the light intensity is sent from the BNC565 digital delay generator to the LDC202 external modulation input that controls the laser current (see Figure S10). The curves show the delay and rise time of the $405\,\mathrm{nm}$ laser, which is mainly limited by the $200\,\mathrm{kHz}$ bandwidth of the LDC202. The gray lines indicate the 0 to 100 percent rise time at $100\,\mathrm{kW\,m^{-2}}$ intensity. At these light intensities, the delay is less than $5\,\mu\mathrm{s}$ and the rise time less than $3\,\mu\mathrm{s}$.

The gated cantilever clock circuit used an AD790 comparator, with $55\,\mathrm{mV}$ of hysteresis added to prevent unwanted oscillations, to convert the sine wave to a square wave clock signal. The square wave was input to the latch enable pin ($\overline{\mathrm{LE}}$) of a transparent D-type latch (CD74HC563E) and a NOR gate (CD4001BE). The output ($\overline{\mathrm{Q}}$) is transparent to the input when the latch enable is high. The digital PCI-6259 signal was sent to a data pin of the latch. The latch prevented a partial pulse (not phase locked to the cantilever oscillation) from being triggered when the PCI-6259 output went high while the cantilever clock was also high.

To verify that the measured photocapacitance rise times were caused by the sample, and were not an artifact, we measured or estimated the rise times of the laser and the cabling carrying voltage to the cantilever tip. The laser rise time, with the same settings used in the experiment, was verified using a high-speed photodetector (Thorlabs DET02AFC) and measuring the detector voltage drop through a $50\,\Omega$ terminating resistor on a $70\,\mathrm{MHz}$ bandwidth oscilloscope. The results for 30 and $100\,\mathrm{kW\,m^{-2}}$ estimated intensity are shown in Fig. S11. The rise time was $< 3\,\mu\mathrm{s}$, consistent with the current source's stated $200\,\mathrm{kHz}$ bandwidth, and much faster than the $40\,\mu\mathrm{s}$ (and slower) rise times observed in the sample.

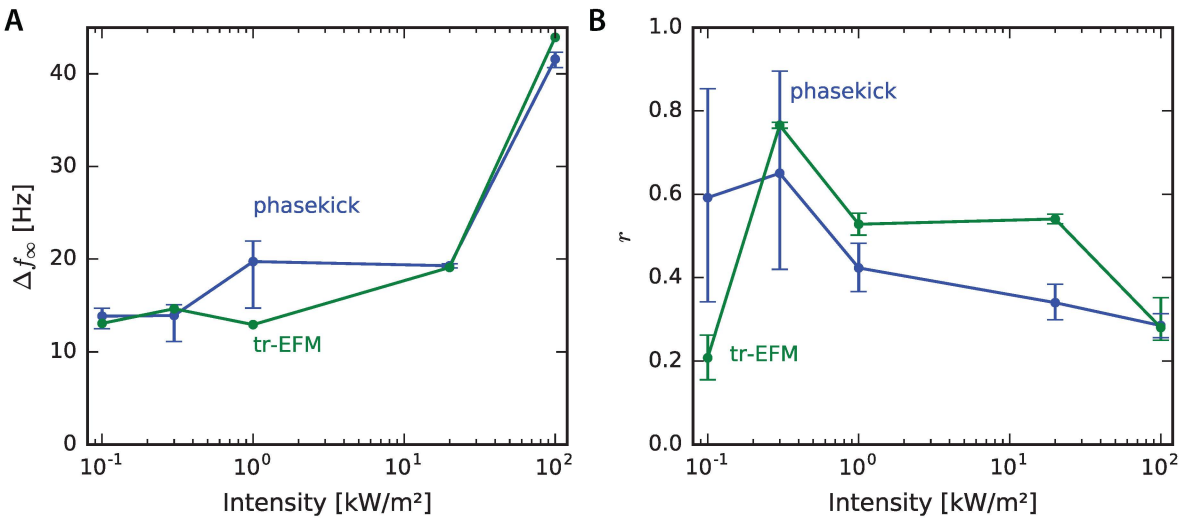

FIG. S12. **Additional comparison of pk-EFM and tr-EFM steady-state photocapacitance** (PFB:F8BT on ITO, $h = 250\,\mathrm{nm}$). (**A**) Steady state photocapacitance *versus* light intensity. (**B**) Fraction of the total steady state capacitance associated with the faster time constant. See time constants τ_1 and τ_2 in Fig. 4D.

The tip charge rise time was more difficult to measure independently. The applied voltage traveled through $3.5\,\mathrm{m}$ of 19-wire cable and $2\,\mathrm{m}$ of 36 AWG wire before reaching the cantilever tip. The total tip voltage cabling capacitance was $\sim 1.3\,\mathrm{nF}$. The BNC565 pulse generator had a current drive ability of $120\,\mathrm{mA}$ and a $50\,\Omega$ output impedance. The output impedance and the cabling capacitor form a low-pass filter with an estimated cutoff frequency of $2.4\,\mathrm{MHz}$ and the BNC565 current drive capability limited slew rates to $90\,\mathrm{V\,\mu s^{-1}}$. By applying short duration tip voltages to the cantilever (Fig. 6D), we determined a tip charge rise time of $35\,\mathrm{ns}$.

S13. CURVE FITTING USING PYSTAN

20,000 posterior samples were used for analysis. These samples were generated as 4 independent chains of 5000 samples each. The potential chain reduction statistic (< 1.01 for all parameters) and trace plots (Fig. S13) were used to discern convergence [64]. Kernel density estimates were calculated using seaborn [65].

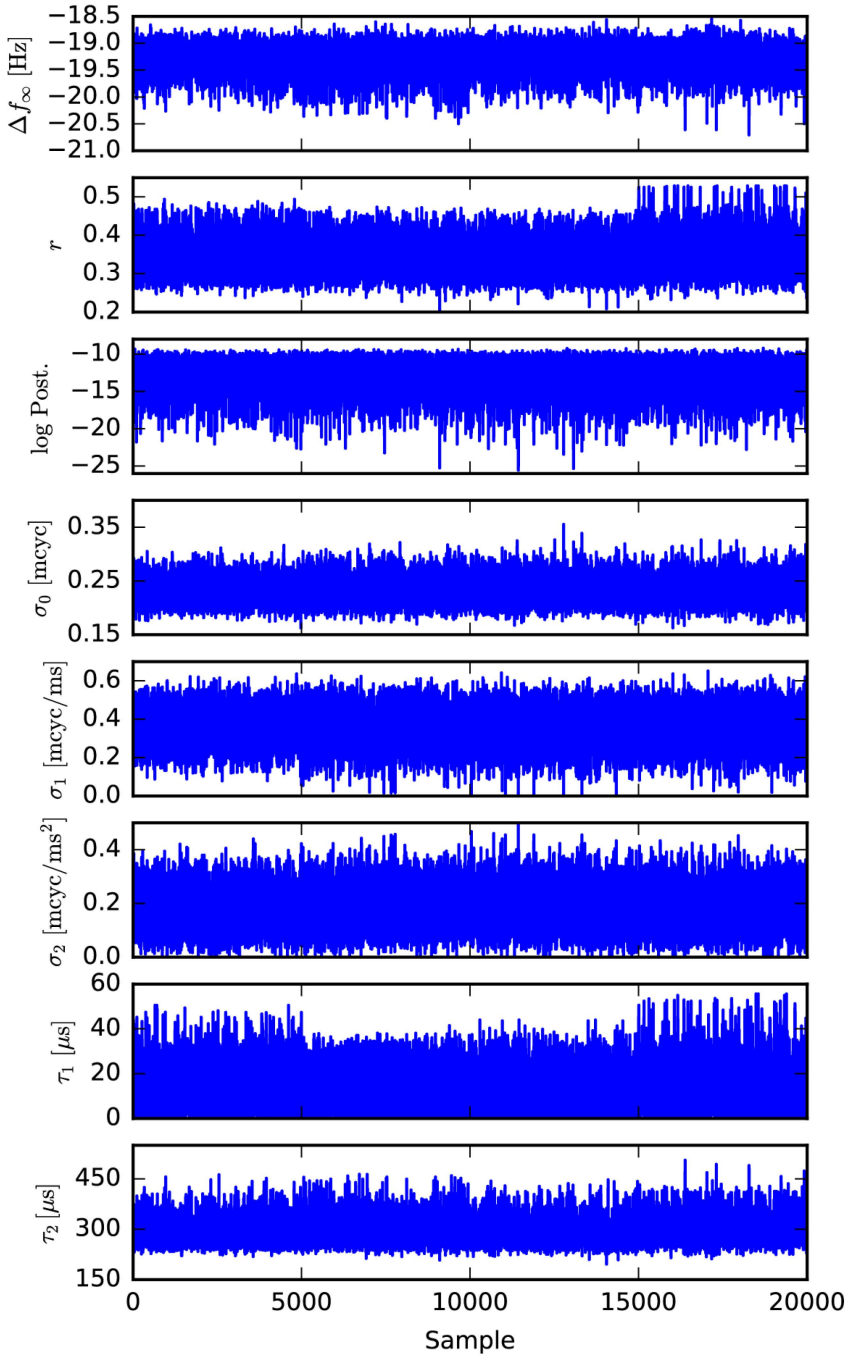

FIG. S13. **PyStan sampling traces**. Traces showing parameter values for PyStan samples of posterior distributions from the $20\,\mathrm{kW\,m^{-2}}$ pk-EFM dataset. Samples from each chain (4 of 5000 samples each) are arranged sequentially.

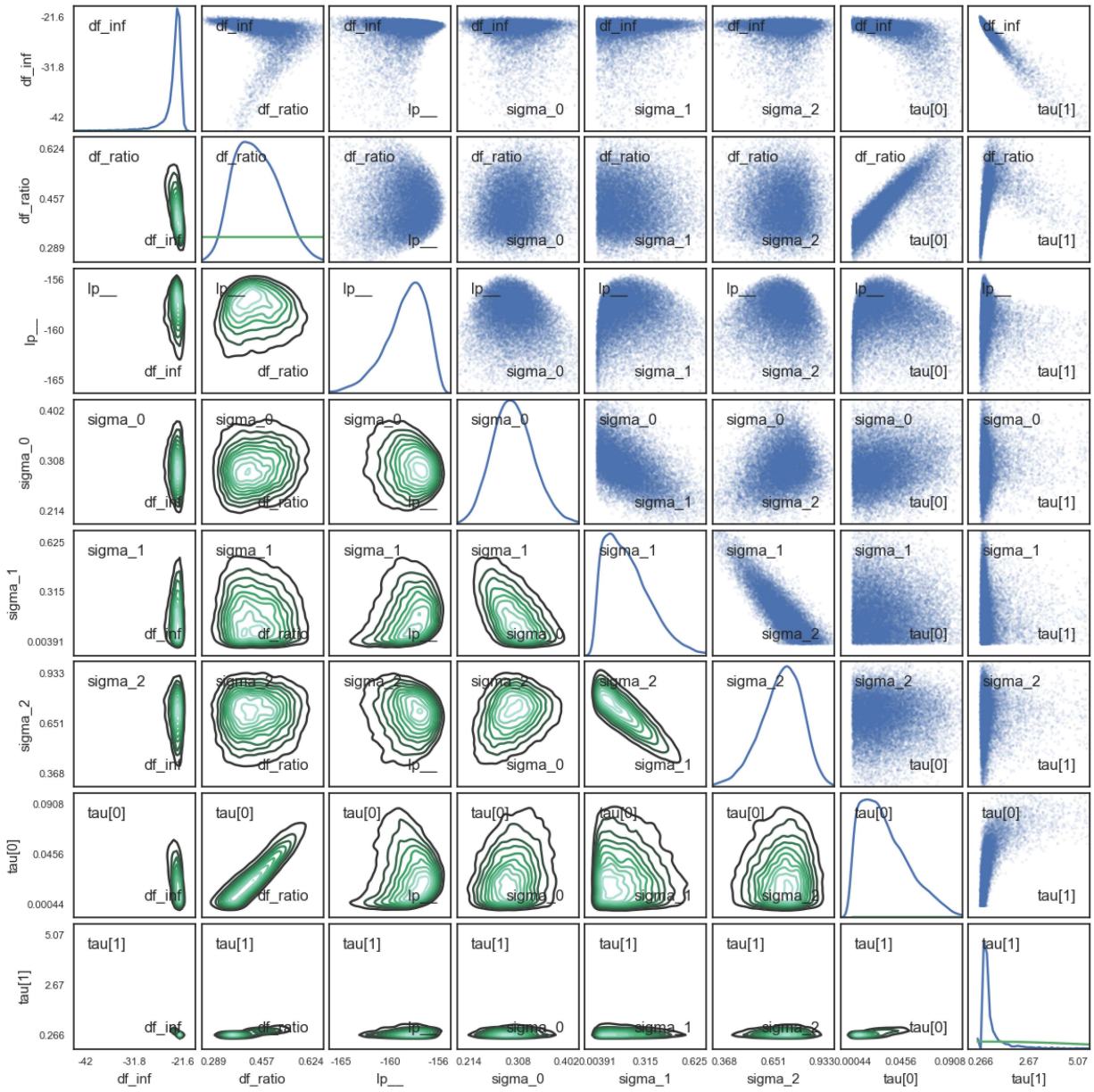

FIG. S14. **pk-EFM posterior distribution samples**. Pair plots illustrating the posterior distribution and correlations between parameters from the $20\,\mathrm{kW\,m^{-2}}$ pk-EFM dataset, estimated using $N = 20000$ samples. On the diagonal, a kernel density estimator (blue) shows the posterior distribution along with prior distribution (green). Parameter correlations are shown by plotting the samples (above diagonal) and using a 2D kernel-density estimator (below diagonal). The time constant τ is in units of milliseconds.

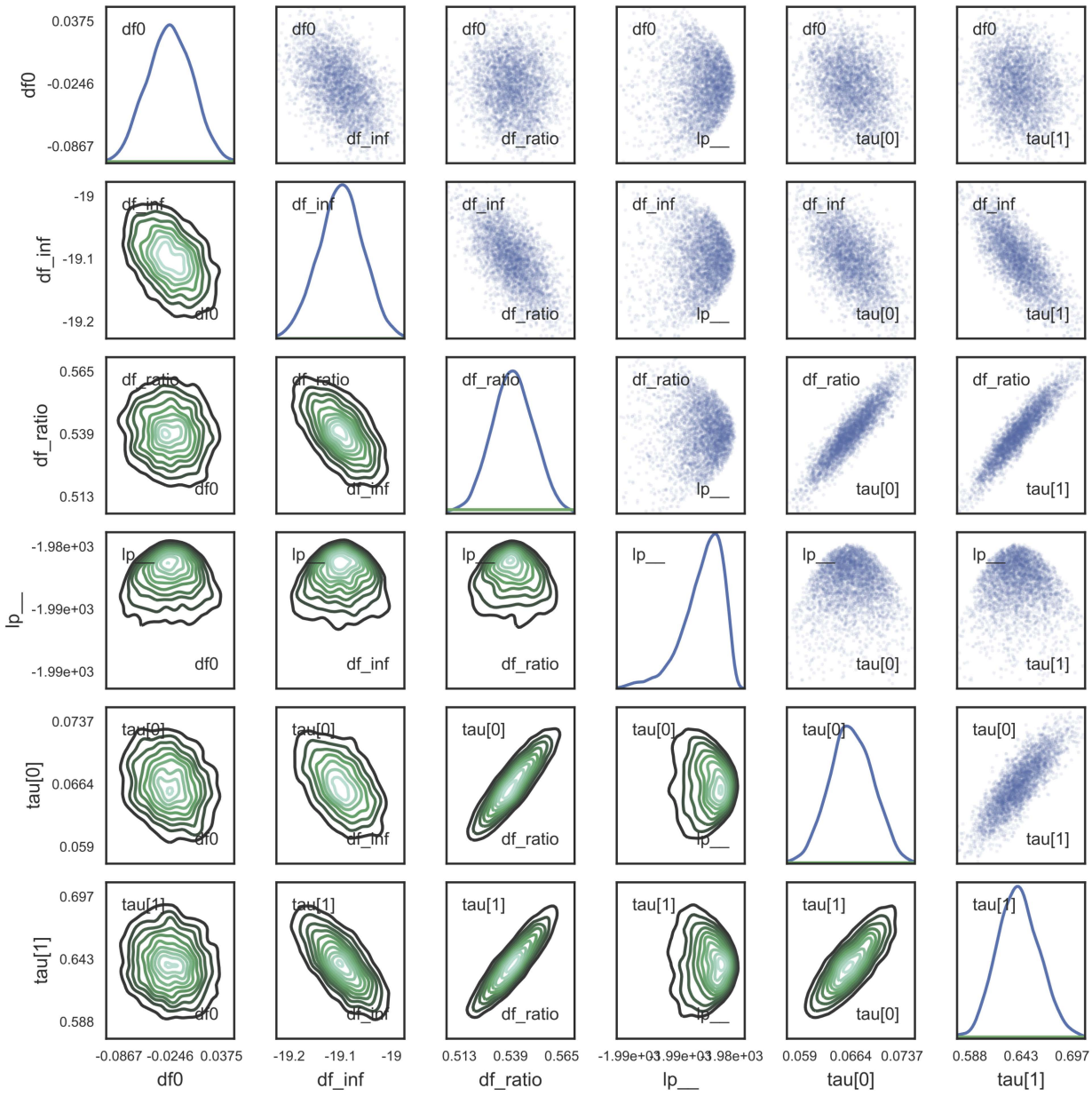

FIG. S15. **tr-EFM posterior distribution samples**. Pair plots illustrating the posterior distribution and correlations between parameters from the $20\,\mathrm{kW\,m^{-2}}$ tr-EFM dataset, estimated using $N = 6000$ samples. On the diagonal, a kernel density estimator (blue) shows the posterior distribution along with prior distribution (green). Parameter correlations are shown by plotting the samples (above diagonal) and using a 2D kernel-density estimator (below diagonal). The time constant τ is in units of milliseconds.